

On recovering distributed IP information from inductive source time domain electromagnetic data

Seogi Kang and Douglas W. Oldenburg

Department of Earth, Ocean and Atmospheric Sciences, University of British Columbia, B.C. V6T 1Z4, Canada

SUMMARY

We develop a procedure to invert time domain induced polarization (IP) data for inductive sources. Our approach based upon the inversion methodology in electrical IP (EIP), which uses linear sensitivity function, although careful treatments are required for inductive source IP (ISIP). The principal difference of inductive source IP (ISIP) from conventional EIP is the absence of steady-state electric field. After turn-off of the current, the amplitude of the electric field starts from zero, reaches to peak then decays. This different excitation mechanism will increase the complexity in polarization currents (i.e. vortex currents in a conductor). Thus, this difference should be incorporated in the linearization, and we effectively incorporate this using a proper reference electric field. Because data type for inductive source is usually either magnetic field or its time derivative, we use Biot-Savart law to generate linearized sensitivity function. Our inversion procedure has three following steps: 1) Invert TEM data and recover 3D distribution of conductivity. 2) To decouple IP responses embedded in the observations, we forward model TEM data and subtract this from the observations. Since the recovered conductivity is not correct, computed IP responses may include some residual fields, which possibly need to be removed with some post-processings. 3) By using linearized sensitivity function, we apply 3D IP inversion to each time channel and recover pseudo-chargeability. Post-interpretation of recovered pseudo-chargeability at multiple times allows us to recover intrinsic Cole-

Cole parameters such as time constant and chargeability. Although we mostly focused on airborne time domain EM (ATEM) data with coincident-loop configuration due to its distinctive IP signature in practice: negative response, the IP inversion procedure we design are generic can be applied to different types of TEM survey. With numerical examples, we systematically test the capability of the linearization for ISIP responses for different conductivity structures. Although the linearization was successful for each transmitter, different pseudo-chargeability for each transmitter was a critical issue to proceed inversion for ATEM data. By deriving an effective pseudo-chargeability, which represents every pseudo-chargeability from different transmitters, and testing this, we successfully dealt with this issue to proceed usual IP inversion. We illustrate our inversion procedure by inverting synthetic ISIP data.

1 INTRODUCTION

The electrical conductivity of earth materials can be frequency dependent with the effective conductivity decreasing with decreasing frequency due to the buildup of electric charges that occur under the application of an electric field. Effectively, the rock is electrically polarized. Application of this induced polarization (IP) technique has been particularly successful in mineral exploration for disseminated sulphide or porphyry deposits (Pelton et al. (1978); Fink et al. (1990)). Successes of the IP technique has been shown in geotechnical and environmental problems as well (Kemna et al. (2012)). Polarization charges can accumulate whenever there is an electric field in a medium. In controlled source surveys, the transmitter can be a galvanic source (a generator attached to two grounded electrodes), or an inductive source (arising from current flowing in a wire loop). Most of the researches and applications have focused upon using grounded electrodes and measuring electric fields called EIP survey (Seigel (1959)). Magnetic fields arising from polarization currents (MIP survey) have also been successfully used, particularly in mineral exploration geologies characterized by a conductive overburden (Seigel (1974)). In recent years attention has also turned towards the use of inductive sources. (reasons: resistive overburden difficult to put current into the ground; also for airborne surveys there is no choice). Inductive source IP (ISIP), can have transmitters in the air or on the ground and the waveforms can be in either the frequency or time domain. Recently (Marchant et al. (2012)) showed how, by collecting data at two frequencies, it was possible to measure a datum that depended purely on IP signals and that these data can be inverted to recover a 3D distribution of chargeability. For time domain systems the observations of negative transients in coincident loop systems provide an distinctive

verification of chargeable material (Weidelt (1982)). These negative transients have been frequently observed (Smith & Klein (1996); Kratzer & Macnae (2012); Kang & W. Oldenburg (2015)). In addition, effects of chargeable objects on time domain system with inductive source has been carefully investigated (Smith et al. (1988); Flis et al. (1989); ElKaliouby & Eldiwany (2004); Marchant et al. (2014)).

Extracting information about the complex conductivity can be done in a variety of ways. In principle it can be solved by finding a function $\sigma(x, y, z, \omega)$ or parameterizing the complex conductivity, usually with a Cole-Cole type model, and finding the distribution of those parameters (Yuval & Oldenburg (1997); Hördt et al. (2006)). Traditionally, however, with EIP and time domain waveforms, one first estimates the background conductivity from the asymptotic on-time data and then inverts off-time data to recover information about “chargeability” (Oldenburg & Li (1994)). This is carried out by solving an inverse problem using a linear function where the sensitivities depend upon geometry of the survey and the background conductivity. The recovered values are really pseudo-chargeability, and they have the same units as the data (eg. msec, mV/V). The same procedure can be used in frequency domain experiments but the data might have units of mrad and pfe (percent frequency effect). Inversion of IP data to recover 2D or 3D distributions of pseudo-chargeability are now commonly carried out. These inversions delineate locations of high pseudo-chargeability and the geometry of the bodies. MIP data can be inverted with the same methodology (Chen & W. Oldenburg (2003)).

The physical mechanisms by which polarization charges and currents are established in the ground are independent of their type of transmitter and waveform; the important quantity is the time history of the electric field within the earth. The challenge posed by the use of inductive sources is that steady state electric fields are not established inside the earth as they are for EIP or MIP surveys. The electric field at any location will increase to a maximum value and then decrease as the EM wave diffuses through. The EM fields at any position and time depend upon the convolution of the electric field with the time-dependent conductivity of the rock. Unravelling these complexities, and providing a framework for extracting information about IP characteristics of rocks, are issues we address in our paper.

Our procedure involves three principal steps: 1) estimating the 3D background conductivity, 2) carrying out an EM decoupling to produce IP data (d^{IP}), and 3) inverting d^{IP} using a linear functional. Each of these steps requires special attention for inductive source data and approximations are required in order to proceed. We address these as they are encountered. Our paper proceeds as follows. We first outline our decomposition process for obtaining our d^{IP} data, define a pseudo-chargeability, and show how our problem can be linearized. For ATEM surveys with multiple transmitters, we show how to generate a single linear inverse problem that can be solved for an effective pseudo-chargeability.

The data and pseudo-chargeability are linearly related through the Biot-Savart law and hence a depth weighting, required for other potential field inversions, is necessary to obtain geologic solutions. The inversion can be carried out at multiple times and a pseudo-chargeability as function of time can be generated. These results can be used to recover intrinsic decays of the chargeable rock units and thus potentially differentiate between rock types in the same manner as carried out by Yuval & Oldenburg (1997) using EIP data. In our numerical experiments, we investigate the above steps and procedures, test our assumptions, and evaluate the circumstances under which our technique might provide meaningful results. Although we focus upon airborne TEM data, the analysis we present here is valid for surveys on the earth's surface using inductive sources and also for grounded sources although many of the complications we deal with are not relevant.

2 COMPLEX CONDUCTIVITY

An often-used representation for complex conductivity in the frequency domain is the Cole-Cole model Cole & Cole (1941):

$$\sigma(\omega) = \sigma_{\infty} - \sigma_{\infty} \frac{\eta}{1 + (1 - \eta)(i\omega\tau)^c} = \sigma_{\infty} + \Delta\sigma(\omega), \quad (1)$$

where σ_{∞} is the conductivity at infinite frequency, η is the intrinsic chargeability, τ is the time constant and c is the frequency dependency. Real and imaginary parts of complex conductivity in frequency domain are shown in Figure 1(a) with Cole-Cole parameters: $\sigma_{\infty} = 10^{-2}$ S/m, $\eta = 0.5$, $\tau = 0.01$, and $c=1$. By applying inverse Fourier transform with time dependency, $e^{i\omega t}$, we have

$$\sigma(t) = \mathcal{F}^{-1}[\sigma(\omega)] = \sigma_{\infty}\delta(t) + \Delta\sigma(t), \quad (2)$$

where $\delta(t)$ is Dirac delta function, and $\mathcal{F}^{-1}[\cdot]$ is inverse Fourier transform operator. We rewrite $\Delta\sigma(t)$ as

$$\Delta\sigma(t) = -\sigma_{\infty}\tilde{\eta}^I(t), \quad (3)$$

where intrinsic pseudo-chargeability, $\tilde{\eta}^I(t)$ is defined as

$$\tilde{\eta}^I(t) = -\frac{\Delta\sigma(t)}{\sigma_{\infty}}. \quad (4)$$

Cole-Cole model in time domain is also shown in Figure 1(b). Used Cole-Cole parameters here are same as the above.

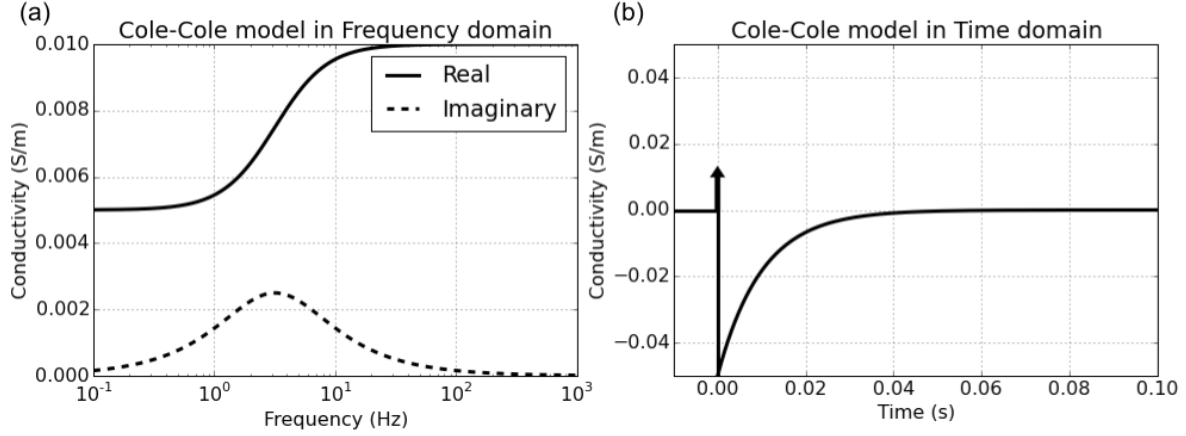


Figure 1. Cole-Cole model in frequency domain (a) and time (b) domain. Used Cole-Cole parameters are $\sigma_\infty = 10^{-2}$ S/m, $\eta = 0.5$, $\tau = 0.01$, and $c=1$.

3 DECOMPOSITION OF OBSERVED RESPONSES

IP effects in the observed data are coupled with EM effects. We need to decompose these effects in the observation to isolate only data associated with the IP phenomena. Maxwell's equations in time domain with a quasi-static approximation are written as:

$$\vec{\nabla} \times \vec{e} = -\frac{\partial \vec{b}}{\partial t}, \quad (5)$$

$$\vec{\nabla} \times \frac{1}{\mu} \vec{b} - \vec{j} = \vec{j}_s, \quad (6)$$

where \vec{e} is the electric field (V/m), \vec{b} is the magnetic flux density (Wb/m²) and μ is the magnetic permeability (H/m). Here \vec{j} is the conduction current. In the frequency domain, this conduction current, \vec{J} is related to conductivity via Ohms law: $\vec{J}(\omega) = \sigma(\omega) \vec{E}(\omega)$ where \vec{E} is the electric field. Converting this relationship to time domain using the inverse Fourier transform yields:

$$\vec{j}(t) = \sigma(t) \otimes \vec{e}(t) = \int_0^t \sigma(u) \vec{e}(t-u) du. \quad (7)$$

where \otimes indicates time convolution for a causal signal. Thus the current density depends upon the previous history of the electric field. As in Smith et al. (1988), we let total fields as $\vec{e} = \vec{e}^F + \vec{e}^{IP}$, $\vec{b} = \vec{b}^F + \vec{b}^{IP}$ and $\vec{j} = \vec{j}^F + \vec{j}^{IP}$, where superscript F indicates fundamental and IP is induced polarization. Here fundamental fields indicate EM fields without IP effects. Substituting into equations (5) and (6) yields the following sequences:

$$\vec{\nabla} \times (\vec{e}^F + \vec{e}^{IP}) = -\frac{\partial}{\partial t} (\vec{b}^F + \vec{b}^{IP}), \quad (8)$$

$$\vec{\nabla} \times \frac{1}{\mu} (\vec{b}^F + \vec{b}^{IP}) - (\vec{j}^F + \vec{j}^{IP}) = \vec{j}_s. \quad (9)$$

The fundamental equations can be written as

$$\vec{\nabla} \times \vec{e}^F = -\frac{\partial \vec{b}^F}{\partial t}, \quad (10)$$

$$\vec{\nabla} \times \frac{1}{\mu} \vec{b}^F - \vec{j}^F = \vec{j}_s. \quad (11)$$

Here

$$\vec{j}^F = \sigma_\infty \vec{e}^F. \quad (12)$$

Substituting the fundamental fields into equations (5) and (6) yields the expressions for the IP fields

$$\vec{\nabla} \times \vec{e}^{IP} = -\frac{\partial \vec{b}^{IP}}{\partial t}, \quad (13)$$

$$\vec{\nabla} \times \frac{1}{\mu} \vec{b}^{IP} = \vec{j}^{IP}. \quad (14)$$

Let $F[\cdot]$ denote operator associated with Maxwells equations, and let d denote the observations that include both EM and IP effects. Keeping the same notation, we can obtain $d = d^F + d^{IP}$, where d^F and d^{IP} are fundamental and IP responses, respectively. Based on this, we define the IP datum as

$$d^{IP} = d - d^F = F[\sigma(t)] - F[\sigma_\infty]. \quad (15)$$

Here $F[\sigma_\infty]$ corresponds to the fundamental response (d^F). This subtraction process acts as an EM decoupling process, which removes the EM effects from the measured responses. This is the same procedure that formed the basis of work by Routh & Oldenburg (2001).

4 PSEUDO-CHARGEABILITY FOR INDUCTIVE SOURCES

Combining equations (2) and (7) writing $j(t) = j^F + j^{IP}$ we obtain

$$\vec{j}^{IP} = \sigma_\infty \vec{e}^{IP} + \vec{j}^{pol}, \quad (16)$$

where the polarization current (\vec{j}^{pol}) is

$$\vec{j}^{pol}(t) = \triangle \sigma(t) \otimes \vec{e}(t). \quad (17)$$

If the electric field has different characteristics for the inductive and galvanic sources this will generate different features in the polarization current. We consider two cases: a) galvanic source without EM induction and b) inductive source with EM induction. The first case corresponds to EIP (Seigel (1959)), and the second is ISIP. Figure 2 shows the amplitude of the fundamental electric field (\vec{e}^F) in the earth for those two cases. For the galvanic source, the electric field is instantaneous due to the steady-state electric field (Figure 2 (a)). However, for the inductive source, the electric field in the

off-time is not zero, but increases to a peak and then decays as shown in Figure 2 (b). The polarization current for the two different sources will be significantly affected by these different electric fields. To capture this difference in a linearized kernel for the IP response, we define pseudo-chargeability ($\tilde{\eta}(t)$) as

$$\tilde{\eta}(t) = -\frac{\vec{j}^{pol}(t)}{\vec{j}^{ref}}, \quad (18)$$

where the reference current (\vec{j}^{ref}) is defined as

$$\vec{j}^{ref} = \sigma_{\infty} \vec{e}^{ref}. \quad (19)$$

Here \vec{e}^{ref} is the reference electric field and both \vec{j}^{ref} and \vec{e}^{ref} are static fields that are independent of time. The pseudo-chargeability defined in equation (18) is the ratio of the polarization current to the reference current. This is a small quantity and it plays an essential role in our linearization.

To evaluate the pseudo-chargeability, we have to identify the reference current or reference electric fields. For the EIP case, the electric field, when there is no IP present, is independent of time as shown in Figure 2(a) and any on-time value of the field can serve as a reference. For the inductive source however, the electric field does not achieve a steady-state, but increases to a peak then decreases.

Each pixel in the Earth has its own reference electric field and time thus both \vec{e}^{ref} and t^{ref} have a 3D distribution. For both EIP and ISIP cases, we mathematically present our choice of the reference electric field as

$$\vec{e}^{ref} = \vec{e}^F(t) \otimes \delta(t - t^{ref}). \quad (20)$$

The reference time for the EIP case can be any time in the on-time, because the fundamental electric field for the EIP case does not change in on-time.

By rearranging equation (18), we obtain

$$\vec{j}^{pol} = -\vec{j}^{ref} \tilde{\eta}(t). \quad (21)$$

This states that the polarization current has an opposite direction to the reference current, and is proportional to the pseudo-chargeability ($\tilde{\eta}(t)$). This conceptual model about the polarization current shown in equation (21) is consistent with Seigel (1959)'s result. We note, that for any pixel, even though \vec{e}^{ref} attains the same value for an ISIP survey as for an EIP survey, the pseudo-chargeability resulting from an ISIP survey will be less than that from an EIP survey. We can infer from this that linearization techniques, which have worked so well in EIP problems, should be successful in ISIP problems.

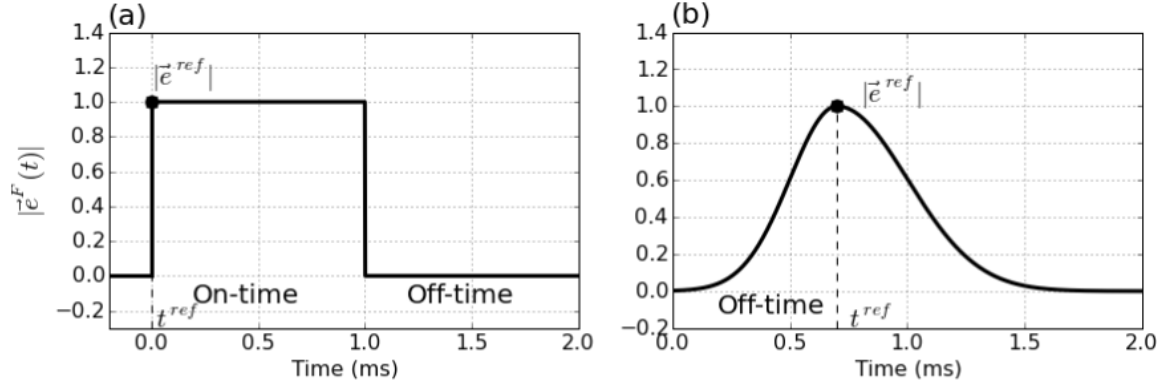


Figure 2. Conceptual diagram for the amplitude of the fundamental electric fields. (a) EIP and (b) ISIP cases.

5 LINEARIZATION

Following from the methodologies in EIP, our goal is to express the IP response (d^{IP}) as a function of the pseudo-chargeability ($\tilde{\eta}(t)$) in time $d^{IP}(t) = J[\tilde{\eta}(t)]$, where $J[\cdot]$ is a linear operator which is independent of time. In doing this we first consider a general EM system which is applicable to galvanic or inductive sources. For any pixel volume in the earth the amplitude and direction of the electric field can vary dramatically in time and this results in a complicated IP charging process. If substantial polarization currents are developed however, they will correspond to a maximum electric field or reference current aligned in a constant direction. Our formulation focuses on this aspect. We assume that the final large scale IP response observed in the data is the result of pixels being charged with an electric field in a specific direction but with a variable amplitude. Let $\vec{e}(t)$ be approximated as

$$\vec{e}(t) \approx \vec{e}^{ref} \hat{w}(t), \quad (22)$$

where $\hat{w}(t)$ is defined as:

$$\hat{w}(t) = P_0[w^{ref}(t)], \quad (23)$$

where a projection ($P_0[\cdot]$) of an arbitrary function, $f(t)$ is

$$P_0[f(t)] = \begin{cases} f(t) & f(t) \geq 0 \\ 0 & \text{if } f(t) < 0, \end{cases} \quad (24)$$

and

$$w^{ref}(t) = \frac{\vec{e}^F(t) \cdot \vec{e}^{ref}}{\vec{e}^{ref} \cdot \vec{e}^{ref}}. \quad (25)$$

Here $w^{ref}(t)$ is a dimensionless function that prescribes the time history of the electric field at each location along the direction of the chosen reference electric field (\vec{e}^{ref}). Negative values of $w^{ref}(t)$ are set to zero in accordance with our conceptual model that polarization currents have an opposite

direction to the reference current (equation (21)). We redefine the pseudo-chargeability as

$$\tilde{\eta}(t) = \tilde{\eta}^I(t) \otimes \hat{w}(t). \quad (26)$$

The polarization current, \vec{j}^{pol} can be approximated with equation (4) as

$$\vec{j}^{pol}(t) \approx -\tilde{\eta}^I(t) \otimes \hat{w}(t) \vec{j}^{ref}. \quad (27)$$

Substituting this into equation (16) yields

$$\vec{j}^{IP}(t) \approx \sigma_\infty \vec{e}^{IP}(t) - \tilde{\eta}^I(t) \otimes \hat{w}(t) \vec{j}^{ref} \quad (28)$$

and this yields

$$\vec{j}^{IP}(t) \approx \sigma_\infty \vec{e}^{IP}(t) - \vec{j}^{ref} \tilde{\eta}(t). \quad (29)$$

The first term, $\sigma_\infty \vec{e}^{IP}(t)$ is usually omitted (Smith et al. (1988)). Here we include it and explore the conditions in which it is important. Because the reference current is static, any time-dependency in the polarization currents is encapsulated in the pseudo-chargeability. The buildup and decrease of polarization currents is a slow process and we assume therefore that this process does not produce induction effects ($\frac{\partial \vec{b}^{IP}}{\partial t} \approx 0$) and therefore we can write

$$\vec{e}^{IP} \approx \vec{e}_{approx}^{IP} = -\vec{\nabla} \phi^{IP}. \quad (30)$$

By taking the divergence of equation (29), substituting \vec{e}^{IP} with equation (30), and carrying out some linear algebra, we obtain

$$\phi^{IP}(t) \approx -[\nabla \cdot \sigma_\infty \vec{\nabla}]^{-1} \nabla \cdot \vec{j}^{ref} \tilde{\eta}(t). \quad (31)$$

By applying the gradient we obtain

$$\vec{e}_{approx}^{IP} = \vec{\nabla} [\nabla \cdot \sigma_\infty \vec{\nabla}]^{-1} \nabla \cdot \vec{j}^{ref} \tilde{\eta}(t). \quad (32)$$

Thus, the electric field due to the IP effect can be expressed as a function of $\tilde{\eta}(t)$ in time. This form is also applicable to the EIP case.

For an inductive source, the data is often either \vec{b} or its time derivative and hence we also need to compute \vec{b}^{IP} or its time derivative. For this, we first compute \vec{j}^{IP} then use the Biot-Savart law to compute \vec{b}^{IP} or $\frac{\partial \vec{b}^{IP}}{\partial t}$. By substituting equation (32) into equation (29), the approximated IP current density, \vec{j}_{approx}^{IP} can be expressed as

$$\vec{j}^{IP}(t) \approx \vec{j}_{approx}^{IP} = \bar{S} \vec{j}^{ref} \tilde{\eta}(t), \quad (33)$$

where

$$\bar{S} = \sigma_\infty \vec{\nabla} [\nabla \cdot \sigma_\infty \vec{\nabla}]^{-1} \nabla \cdot -\bar{I} \quad (34)$$

and \bar{I} is an identity tensor. Applying Biot-Savart law we have:

$$\vec{b}_{approx}^{IP}(\vec{r}; t) = \frac{\mu_0}{4\pi} \int_{\Omega} \frac{\bar{S} \vec{j}^{ref}(\vec{r}_s) \times \hat{r}}{|\vec{r} - \vec{r}_s|^2} \tilde{\eta}(t) d\vec{r}_s. \quad (35)$$

If $\sigma_{\infty} \vec{e}^{IP}$ is omitted in \vec{j}^{IP} then the tensor, \bar{S} becomes $-\bar{I}$. In this situation, the IP current is same as the polarization current, and it always has opposite direction to the reference current. This reversed current, along with Biot-Savart law, provides a physical understanding about the negative transients in ATEM data when the earth is chargeable.

Observed data are often the time derivative of \vec{b} , hence by taking time derivative to the equation (35), we obtain

$$-\frac{\partial \vec{b}_{approx}^{IP}}{\partial t}(\vec{r}; t) = \frac{\mu_0}{4\pi} \int_{\Omega} \frac{\bar{S} \vec{j}^{ref}(\vec{r}_s) \times \hat{r}}{|\vec{r} - \vec{r}_s|^2} \left(-\frac{\partial \tilde{\eta}(t)}{\partial t} \right) d\vec{r}_s. \quad (36)$$

Here we have chosen to keep the minus signs in equation (36) so that $-\frac{\partial \tilde{\eta}(t)}{\partial t}$ is positive when $\tilde{\eta}(t)$ is decaying in time. Accordingly, the IP datum is given by $-\frac{\partial \vec{b}^{IP}}{\partial t}$.

The IP fields shown in equations (32), (35) and (36) are linear functionals of $\tilde{\eta}(t)$ and the equations can be discretized in space as

$$\mathbf{d}_i^{IP} = \mathbf{J} \tilde{\eta}_i, \quad (37)$$

where \mathbf{J} is corresponding sensitivity matrix and the subscript i indicates i^{th} time channel. In particular when the observed datum is the time derivative of \vec{b} , the linear relationship can be written as

$$\mathbf{d}_i^{IP} = \mathbf{J} \left(-\frac{\partial \tilde{\eta}}{\partial t} \Big|_i \right). \quad (38)$$

A detailed description for the discretization of the linearized kernel is shown in sections A and B. The representation in equation (37) is valid for galvanic and inductive sources but the two assumptions: a) $\vec{e} \approx \vec{e}^{ref} \hat{w}(t)$ and b) $\vec{e}^{IP} \approx -\vec{\nabla} \phi^{IP}$ need to be tested numerically for the case of inductive sources.

6 IP INVERSION METHODOLOGY

6.1 3D IP inversion with a linearized kernel

The linear inverse problem to recover chargeability is straightforward and is described in Oldenburg & Li (1994). We rewrite equation (37) as

$$\mathbf{d}^{pred} = \mathbf{J} \mathbf{m}, \quad (39)$$

where \mathbf{J} is the sensitivity matrix of linear problem, which corresponds to \mathbf{J} shown in equation (37). Here, \mathbf{d}^{pred} is IP responses at i^{th} time channel (\mathbf{d}_i^{IP}), \mathbf{m} is distributed model parameters, which can be either $\tilde{\eta}_i$ or $-\frac{\partial \tilde{\eta}}{\partial t} \Big|_i$. In our work here we invert each time channel of d^{IP} , separately.

The solution to the inverse problem is the model \mathbf{m} that solves the optimization problem

$$\text{minimize } \phi = \phi_d(\mathbf{m}) + \beta\phi_m(\mathbf{m}) \text{ s.t. } 0 \leq \mathbf{m},$$

where ϕ_d is a measure of data misfit, ϕ_m is a user-defined model objective function and β is regularization or trade-off parameter. We solve this optimization problem using a projected Gauss-Newton method (Kelley (1999)). The value of β in the iteration of this non-linear inversion is determined using a cooling technique where β is progressively reduced from some high value. The inversion is stopped when the tolerance is reached (cf. Oldenburg & Li (2005); Kang et al. (2014)).

We use the sum of the squares to measure data misfit

$$\phi_d = \|\mathbf{W}_d(\mathbf{A}\mathbf{m} - \mathbf{d}^{obs})\|_2^2 = \sum_{j=1}^N \left(\frac{\mathbf{d}_j^{pred} - \mathbf{d}_j^{obs}}{\epsilon_j} \right)^2, \quad (40)$$

where N is the number of the observed data and \mathbf{W}_d is a diagonal data weighting matrix which contains the reciprocal of the estimated uncertainty of each datum (ϵ_j) on the main diagonal, \mathbf{d}^{obs} is a vector containing the observed data, \mathbf{d}^{pred} is a vector containing calculated data from a linear equation given in equation (39). The model objective function, ϕ_m is a measure of amount structure in the model and upon minimization this will generate a smooth model which is close to a reference model, \mathbf{m}_{ref} . We define ϕ_m as

$$\phi_m = \sum_{i=s,x,y,z} \alpha_i \|\mathbf{W}_i \mathbf{W}(\mathbf{m} - \mathbf{m}_{ref})\|_2^2, \quad (41)$$

where \mathbf{W}_s is a diagonal matrix, and \mathbf{W}_x , \mathbf{W}_y and \mathbf{W}_z are discrete approximations of the first derivative operator in x , y and z directions, respectively. The α 's are weighting parameters that balance the relative importance of producing small or smooth models.

We are inverting each time channel of d^{IP} datum, separately. Thus, we do not have intrinsic depth resolution. This could be overcome if there were multiple receivers for each transmitter. To compensate for this, and similar to the magnetic inversion (Li & Oldenburg (1996)), we apply depth weighting through model weighting matrix (\mathbf{W}):

$$\mathbf{W} = \text{diag}(\mathbf{z} - \mathbf{z}_0)^{1.5}, \quad (42)$$

where \mathbf{z} and \mathbf{z}_0 are discretized depth locations and reference depth in the 3D domain.

6.2 Extracting intrinsic IP parameters

The output of our IP inversion is a 3D distribution of the pseudo-chargeability at multiple time channels. As its name suggests, pseudo-chargeability is not an intrinsic IP parameter like chargeability, but

it is convoluted property between $\tilde{\eta}^I(t)$ and $w^e(t)$:

$$\tilde{\eta}(t) = \tilde{\eta}^I(t) \otimes \hat{w}(t), \quad (43)$$

with the definition of intrinsic pseudo-chargeability (equation (4)). We would now like to use the $\tilde{\eta}(t)$ as the data and recover intrinsic parameters such as η, τ, c in a Cole-Cole model. Assuming a Debye model ($c=1$), we obtain

$$\tilde{\eta}^I(t) = \frac{\eta}{(1-\eta)\tau} e^{-\frac{t}{(1-\eta)\tau}}, \quad (44)$$

Since we have σ_∞ we can compute $\hat{w}(t)$, which is time history of the electric field. Accordingly, we can unravel the recovered pseudo-chargeability to extract intrinsic IP parameters such as chargeability(η) and time constant (τ). We use a gradient-based optimization, we need the sensitivity function for the pseudo-chargeability (equation (43)) with regard to η and τ . To simplify this procedure, we rewrite intrinsic pseudo-chargeability as

$$\tilde{\eta}^I(t) = ae^{-bt}, \quad (45)$$

where $a = \frac{\eta}{(1-\eta)\tau}$ and $b = \frac{1}{(1-\eta)\tau}$. Then we take derivative of $\tilde{\eta}(t)$ with regard to a and b :

$$\frac{\partial \tilde{\eta}(t)}{\partial a} = e^{-bt} \otimes \hat{w}(t), \quad (46)$$

$$\frac{\partial \tilde{\eta}(t)}{\partial b} = -ate^{-bt} \otimes \hat{w}(t). \quad (47)$$

With these sensitivity functions, we can set up an inverse problem, and recover a and b . Chargeability and time constant can be obtained by using a and b :

$$\eta = \frac{a}{b}, \quad (48)$$

$$\tau = \frac{1}{(1 - a/b)b}. \quad (49)$$

We apply this inversion separately to each cell in the recovered pseudo-chargeability in a manner similar to (Yuval & Oldenburg 1997). For the better representation of time-dependent conductivity, a different parameterization such as stretched-exponential (Kohlrausch (1854)) or Cole-Cole model with variable c can be implemented.

6.3 Handling multiple transmitters in ATEM surveys

The work for inductive sources in the previous sections has been developed for a single transmitter and 3D information about chargeability can be obtained if there are multiple receivers. For ATEM data however, we have only a single receiver location for each transmitter but we have multiple transmitter locations. Our goal is to alter the problem to work with an effective pseudo-chargeability.

In our linearized equation (39), each transmitter has its own sensitivity and pseudo-chargeability. For our airborne case the sensitivity for the k -th transmitter is the k -th row of \mathbf{J} and the pseudo-chargeability is $\tilde{\eta}^k$. The corresponding IP datum is

$$d_k^{IP}(t) = \sum_{i=1}^{nC} J_{k,i} \tilde{\eta}_i^k(t), \quad k = 1, \dots, nTx, \quad (50)$$

where nTx is the number of transmitters, nC is the number of cells in the domain, and $J_{k,i}$ indicates an element of the Jacobian matrix for the k -th transmitter and the i -th cell. We want to replace $\tilde{\eta}_i^k$ with a single effective pseudo-chargeability $\tilde{\eta}^k$ and therefore write the IP as

$$d_k^{IP}(t) = \sum_{i=1}^{nC} J_{k,i} \tilde{\eta}_i(t), \quad k = 1, \dots, nTx, \quad (51)$$

The waveforms are different for each transmitter and hence this representation cannot be exact. To examine the implications of this it suffices to look at the contribution of any volumetric pixel. Each pixel contributes to all of the IP data but in differing amounts. The total contribution of the i -th pixel to the nTx data set at a single time is

$$q_i = \sum_{k=1}^{nTx} J_{k,i} \tilde{\eta}_i^k(t), \quad i = 1, \dots, nC. \quad (52)$$

Our goal is to find an effective chargeability that produces the same net effect on the measured data. We search for a transmitter-independent $\tilde{\eta}_i$ such that

$$q_i^{est} = \sum_{k=1}^{nTx} J_{k,i} \tilde{\eta}_i(t), \quad i = 1, \dots, nC. \quad (53)$$

Minimizing the least squares difference between equations (52) and (53) yields

$$\tilde{\eta}_i(t) = \frac{\sum_{k=1}^{nTx} J_{k,i}^2 \tilde{\eta}_i^k(t)}{\sum_{k=1}^{nTx} J_{k,i}^2} = \sum_{k=1}^{nTx} a_i^k \tilde{\eta}_i^k(t), \quad i = 1, \dots, nC. \quad (54)$$

where normalized weight (a_i^k) is

$$a_i^k = \frac{J_{k,i}^2}{\sum_{k=1}^{nTx} J_{k,i}^2}, \quad i = 1, \dots, nC. \quad (55)$$

With the above understanding about how $\tilde{\eta}_i$ relates to the $\tilde{\eta}_i^k$ from each transmitter we can proceed as follows. Firstly, from equation (26) we have

$$\tilde{\eta}_i^k(t) = \tilde{\eta}^I \otimes \hat{w}_i^k(t) \quad (56)$$

as usual (equation (37)). In addition, by letting

$$\tilde{\eta}_i(t) = \tilde{\eta}^I(t) \otimes w_i^e(t), \quad (57)$$

we define effective time history of the electric field, $w_i^e(t)$ as

$$w_i^e(t) = \sum_{k=1}^{nTx} a_i^k \hat{w}_i^k(t), \quad i = 1, \dots, nC. \quad (58)$$

The above equations shows that the pseudo-chargeability for any pixel recovered from the inversion is equal to the convolution of the intrinsic pseudo-chargeability with a time function. Although it is somewhat involved, the time function associated with each pixel can be evaluated by knowing the electric fields associated with the fundamental EM problem. Ultimately this allows us to estimate the parameters associated with the intrinsic pseudo-chargeability in the same manner as outlined for the case with a single transmitter. Our ability to evaluate the time functions and test the validity of equation(51) will be treated in Section 7.5.

6.4 IP inversion procedure

As seen in the previous sections the extraction of IP information from TEM data has multiple steps. These include: (1) invert TEM data and recover a 3D conductivity model (σ_{est}). (2) Forward model σ_{est} to obtain the fundamental response d^F and subtract it from the observations to obtain d^{IP} data. (3) Invert d^{IP} data to recover pseudo-chargeability model at individual time channels using the relationship in equation (37). (4) Further process the inversion outputs at multiple time-channels to estimate the Cole-Cole, or equivalent IP parameters.

In the following we investigate each of the above steps via numerical simulations and test the validity of our assumptions.

7 NUMERICAL EXPERIMENTS

For our numerical experiments we concentrate upon coincident loop ATEM surveys. This choice is made because of the observed negative transients that are direct indicators of IP phenomena (Kratzer & Macnae (2012); Kang & W. Oldenburg (2015); Kang et al. (2015); Oldenburg et al. (????)), and the extensive use of this survey by industry.

We begin with a simple IP model composed of a chargeable block in a half-space as shown in Figure 3. Cole-Cole parameters of block are $\eta = 0.2$, $\tau = 0.005$ and $c = 1$. The conductivity of the half-space, (σ_1) is 10^{-3} S/m, whereas σ_2 , the conductivity at infinite frequency, σ_∞ , for the chargeable body, is variable. We consider three cases: a) canonical ($\sigma_2 = \sigma_1$), b) conductive ($\sigma_2 = 10^2 \times \sigma_1$) and c) resistive models ($\sigma_2 = 10^{-2} \times \sigma_1$). The 3D earth is discretized with $50 \times 50 \times 50$ m core cells and the number of cells in the domain is $41 \times 41 \times 40$. The size of the chargeable body is $250 \times 250 \times 200$ m and the top boundary is located 50 m below the surface. The EMTDIP code (Marchant et al. (2014)) is used

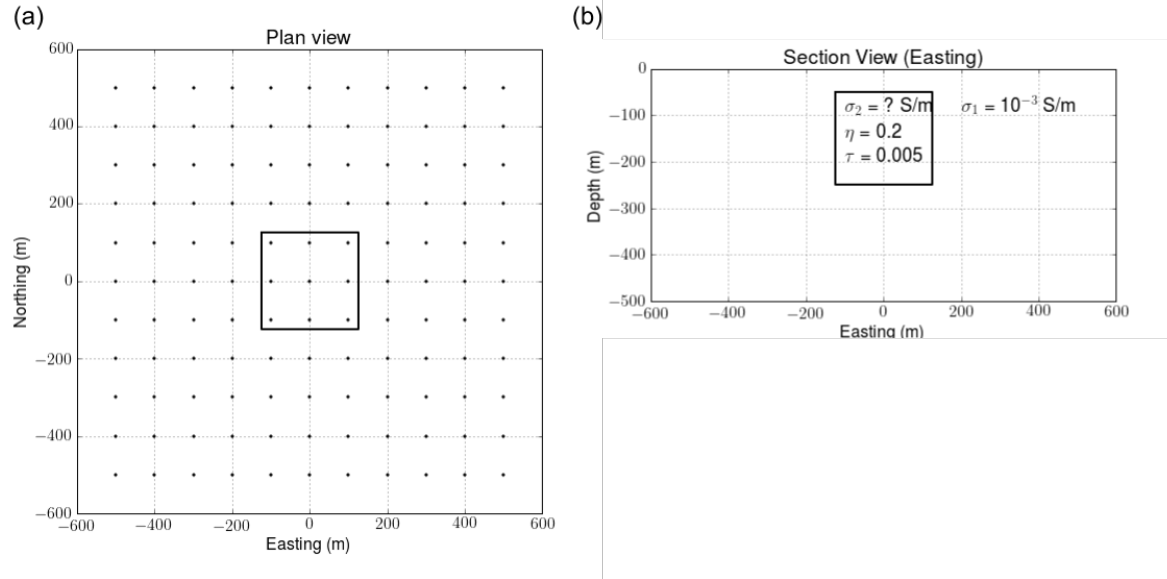


Figure 3. Plan (a) and section b) views of the IP model. Dashed line in (a) contours the boundary of the IP body. Solid circles in (a) denotes the sounding locations.

to compute forward ATEM responses that include IP effects. The survey consisting of 11 soundings along each of 11 lines is shown in Figure 3a. Data are from a coincident-loop system and both Tx and Rx are located 30 m above the surface; the radius of the loop is 10 m. A step-off transmitter waveform is used and the range of the observed time channels is 0.01-60 ms. The observed responses can be either vertical component of \vec{b} or $\frac{\partial \vec{b}}{\partial t}$.

In this section, we first decompose the observed responses and the total currents into fundamental and IP portions to aid in the basic understanding of IP effects in ATEM data. Second, we validate the linearized functional by computing the approximate IP current and IP responses, and compare these with the true values. Third, we investigate the feasibility of an effective pseudo-chargeability in 3D IP inversion. Fourth, we invert the IP data and recover 3D distributions of pseudo-chargeability at multiple times. Lastly, we use the recovered pseudo-chargeabilities to examine the potential to extract intrinsic Cole-Cole parameters.

7.1 IP responses

Using the EMTDIP code and carrying out two simulations, we compute the IP data via subtraction in equation (15). Figure 4 shows the observed, fundamental, and IP responses at a sounding location above the center of the chargeable body for (a) canonical, (b) conductive and (c) resistive models. Both b_z and $-\frac{\partial b_z}{\partial t}$ data are shown. The IP effects are most noticeable for the conductive body and we turn attention to this example first. The IP response starts to significantly affect the observations near 0.6 ms and the observed responses show a sign reversal near 1 ms. Beyond that time the signal is dominated by the IP. The dashed line in Figure 4b shows that after turn-off of the transmitter current, the IP current increases (as inferred by the magnitude of the b_z field) until about 1 ms and then decreases. We interpret this in terms of charging and discharging phases and a vertical dashed line in the figure defines the two phases. In the charging phase at early times the EM effects dominate and IP signals are not expected to be observed. In the discharging phase, which occurs at later time, the IP effects may eventually dominate the EM effects. The maximum of the b_z^{IP} corresponds to the zero crossing for $\frac{\partial b_z^{IP}}{\partial t}$ but the times at which the IP signal becomes dominant are delayed compared to b_z^{IP} . By comparing the observations with the fundamental fields we see that the IP signal could be recognized in the b_z data near 0.7 ms and near 2.0 ms in the $\frac{\partial b_z}{\partial t}$ data.

The plots for the canonical and resistive bodies show that the time that separates charging and discharging occurs earlier than for the conductive body. This is a reflection that the fundamental currents reside for a longer time in a conductor. For the canonical body, a significant difference between the measured responses and the fundamental fields occur about 0.9 ms for b_z and about 2 ms for $\frac{\partial b_z}{\partial t}$. The amplitudes of the IP responses are significantly smaller than those for the conductor. Lastly, there is little IP signal for the resistive body; the IP signal is much smaller than the fundamental response throughout the given time range. This is a consequence of the small fundamental currents in the resistor.

The decay curves from a sounding location provide insight about the IP response but more is gleaned by looking at data from all sounding locations in the ATEM survey. We focus on b_z^{IP} for the conductive block at selected time channels. Figure 5 shows interpolated maps of the observed, fundamental and IP responses at (a) 0.86 ms and (b) 6.7 ms which are respectively included in the charging and discharging times. At 0.86 ms, the observations are dominated by the fundamental response and no negative values, which are the signature of the IP effect, are observed. Subtracting the fundamental however, yields a residual d^{IP} data map that has a strong negative. This example shows that our EM decoupling procedure can work satisfactorily. At 6.7 ms, obtaining good IP data are easily identified because the observed data already show negative values. There is still a weak fundamental field and the subtraction process improves the d^{IP} response. The d^{IP} data at 0.86 ms and 6.7 ms shown in

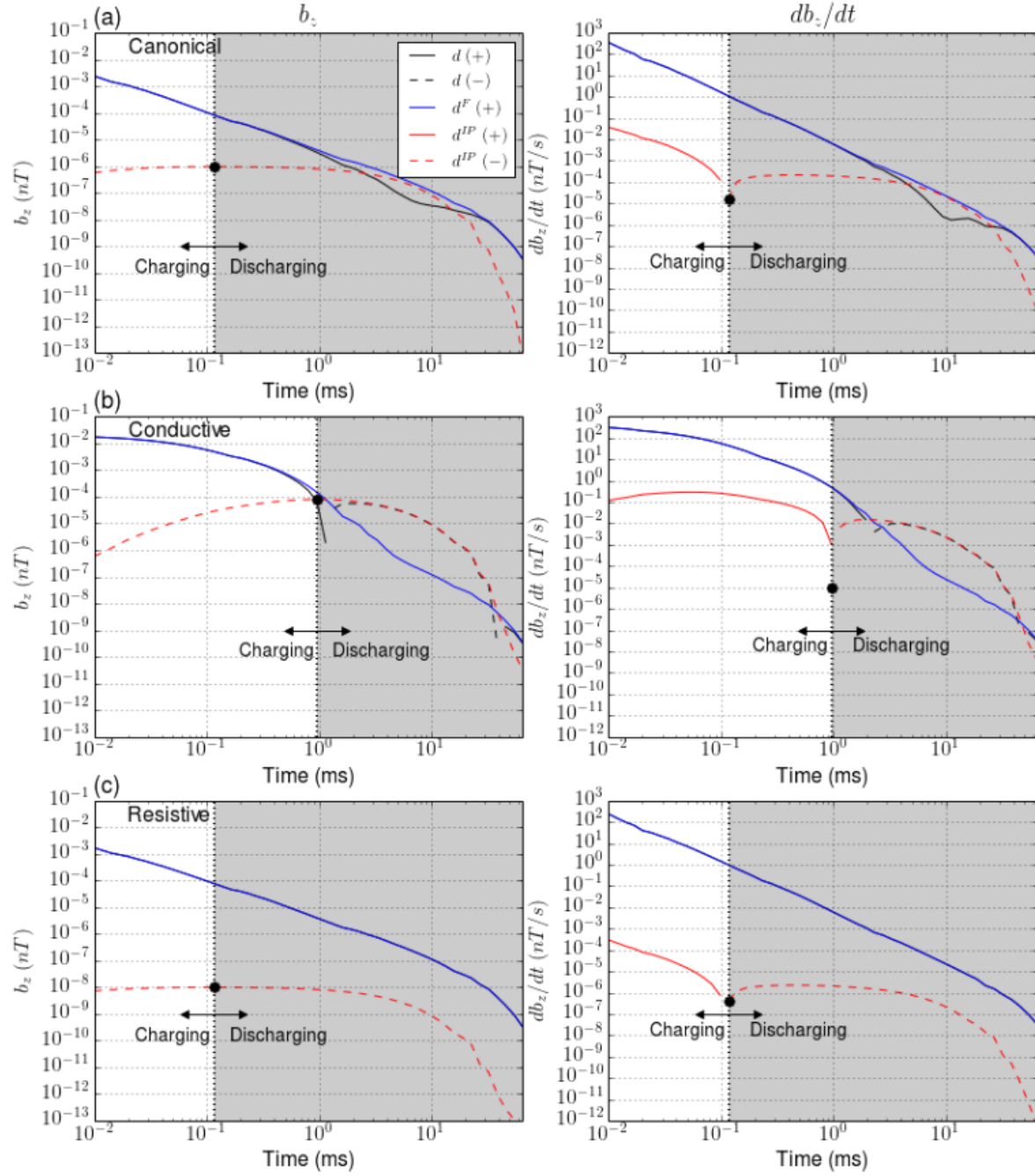


Figure 4. Time decaying curves of the observations (d ; black line), fundamental (d^F ; blue line) and IP (d^{IP} ; red line) responses. All three cases: (a) canonical, (b) conductive and (c) resistive are presented. Right and left panels show b_z and $\frac{\partial b_z}{\partial t}$. Black dotted line indicates the maximum polarization time.

- 1 Figure 5 are of sufficient quality to be inverted. The decoupling has been carried out using the known
- 2 background conductivity σ_∞ which, in reality must be estimated. We address this issue later.

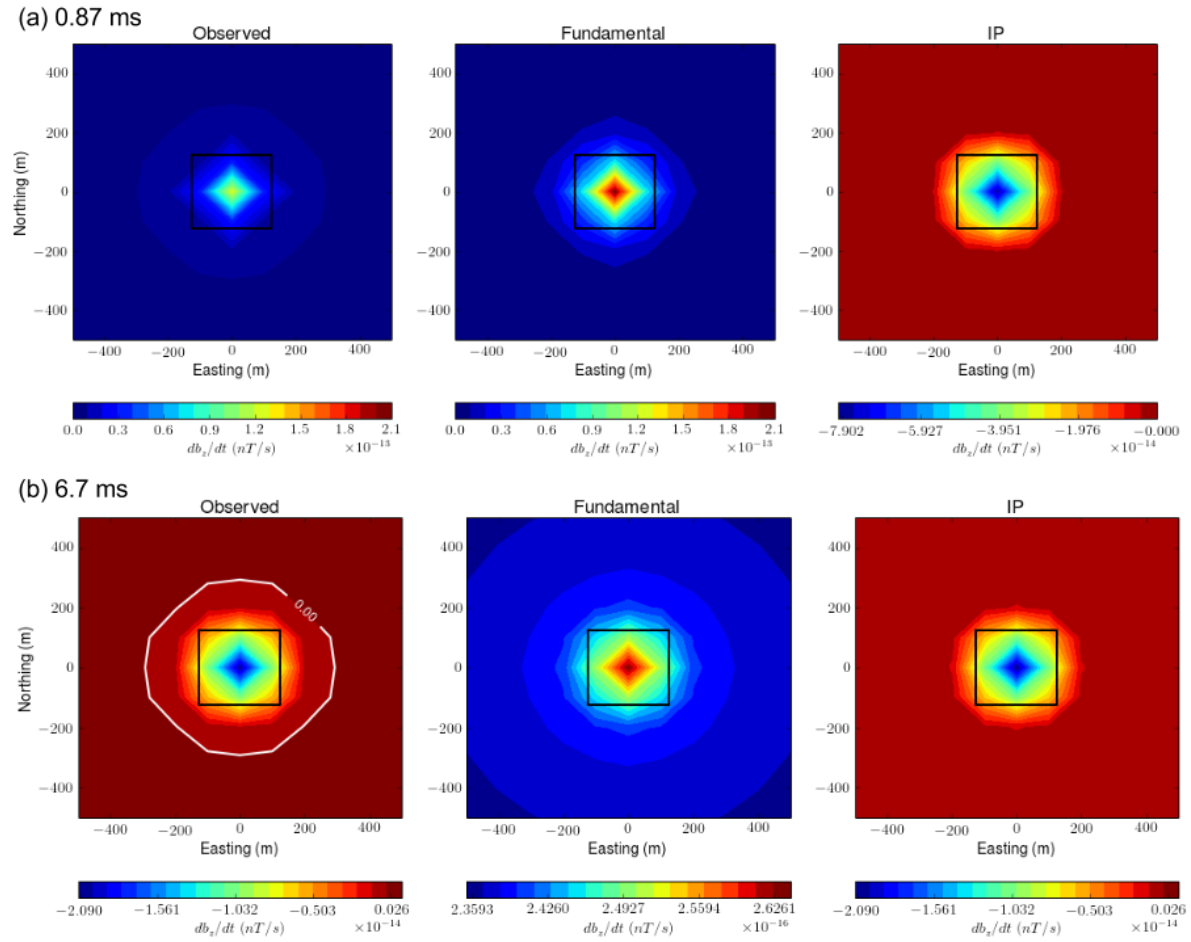


Figure 5. Interpolated maps of observed (left panel), fundamental (middle panel) and IP (right panel) responses. Two time channels at (a) 0.86 ms and (b) 6.7 ms are presented. White line contours zero-crossing line in the observed response.

7.2 Polarization currents

To evaluate the polarization current shown in equation (17) for the linear functional, we assumed $\vec{e}(t) \approx \vec{e}^{ref} w^e(t)$ and defined our reference current as $\vec{j}^{ref} = \sigma_\infty \vec{e}^{ref}$. That yielded our approximation of the polarization current to be yielding $\vec{j}^{pol}(t) \approx -\vec{j}^{ref} \tilde{\eta}(t)$. This approximation states two crucial points: a) a polarization current correspond to a reference current aligned in a constant direction since $\tilde{\eta}(t)$ is scalar property. b) Direction of the polarization current does not change in time. We investigate these by evaluating both reference and polarization currents. From equation (20), the reference current can be considered as the maximum fundamental current occurred in time history. To evaluate polarization currents we rearrange equation (16) as $\vec{j}^{pol} = \vec{j}^{IP} - \sigma_\infty \vec{e}^{IP}$. Computation of this subtraction yields the polarization currents.

Here we limit our attention to canonical and conductive models. Figure 6a and b show reference currents for canonical and conductive models, respectively. A transmitter is located at (-200 m, 0 m, 30 m) and marked as a white solid circle in the figure, where (\cdot, \cdot, \cdot) means a point at (easting, northing, depth). Reference currents for the canonical model are circular, centered to the transmitter location, and is decaying as further away from this location. For conductive model, additional vortex currents induced in the conductor are observed. We compare these reference currents with polarization currents. Figures 7 show the plan and section view maps of the polarization currents at 0.86 ms. Comparisons of Figures 6 and 7 clearly show that polarization currents for both canonical and conductive models are oppositely aligned with reference currents for those models. Figure 8 show polarization currents at 6.7 ms, and direction of polarization currents are similar to those at 0.86 ms. This illustrates that direction of polarization currents after 0.86 ms for both canonical and conductive models are almost constant in time.

For the EIP, we simply expect dipolar IP response originated from the linear-shaped polarization current in a chargeable medium (Seigel (1959)). However, for the ISIP additional complexity arises due to vortex currents induced in a conductor because these generate complicated polarization currents with chargeable medium. Our choice of reference currents effectively incorporates complicated direction of polarization currents for the conductive model.

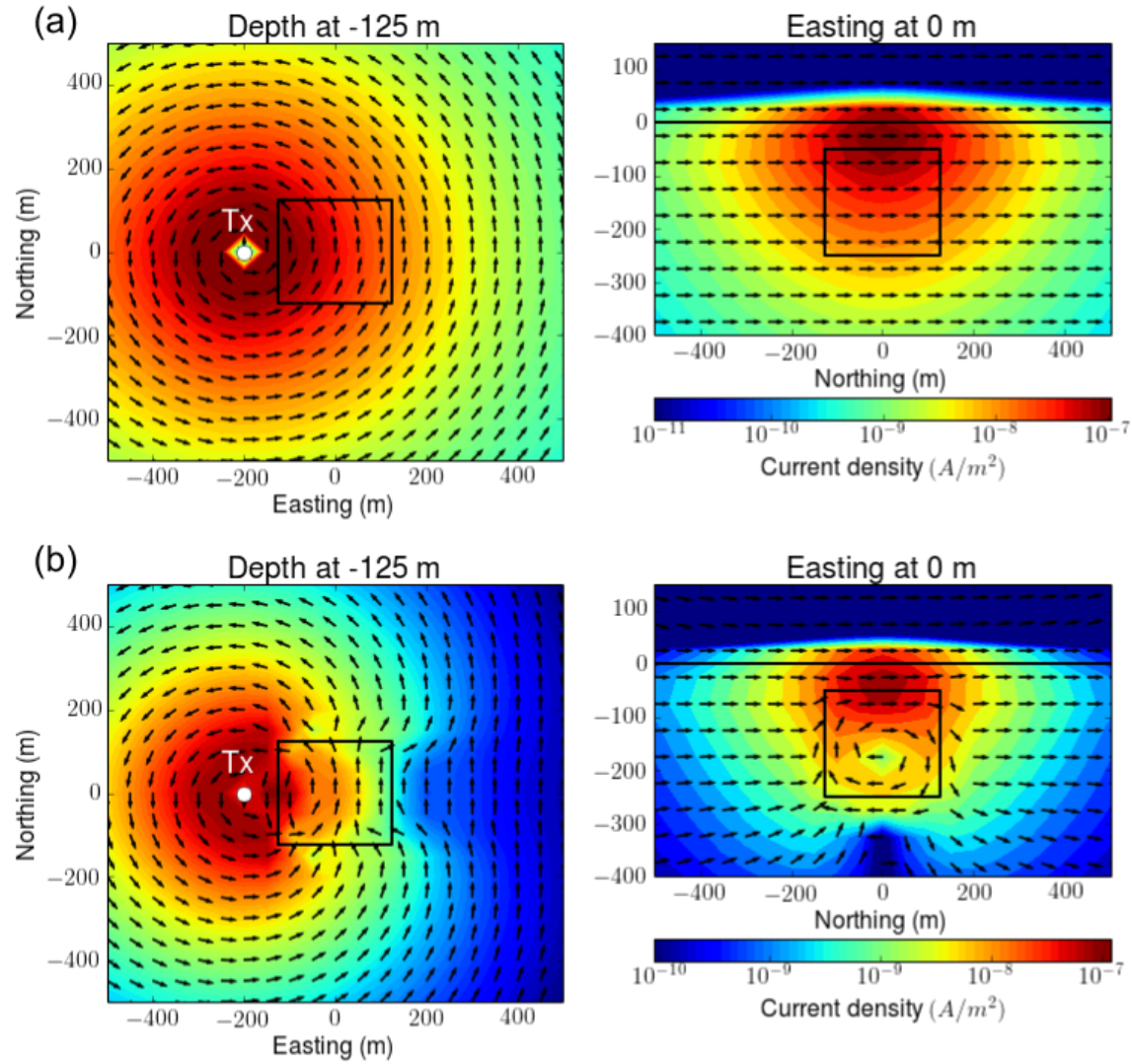


Figure 6. Maps of reference currents: (a) canonical and (b) conductive models. Left and right panel show plan and section views at -125 m-depth and 0 m-easting, respectively. A transmitter is located at (-200 m, 0 m, 30 m). Black arrows and shaded value indicate the direction and amplitude of the current, respectively. Black solid outlines boundary of the surface or the chargeable body.

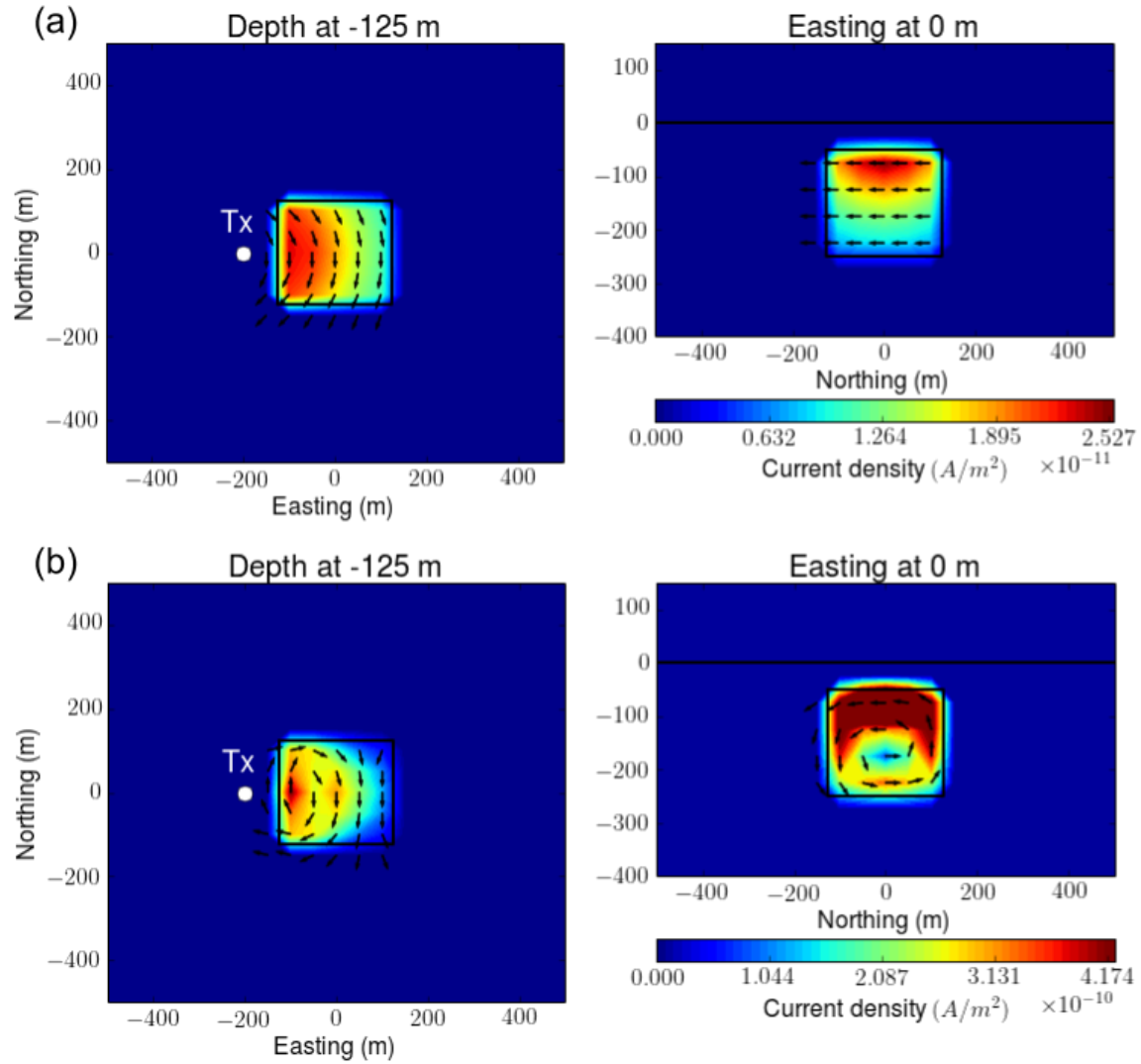


Figure 7. Maps of polarization currents: (a) canonical and (b) conductive models at 0.86 ms. Left and right panel show plan and section views at -125 m-depth and 0 m-easting, respectively. A transmitter is located at (-200 m, 0 m, 30 m). Black arrows and shaded value indicate the direction and amplitude of the current, respectively. Black solid outlines boundary of the surface or the chargeable body.

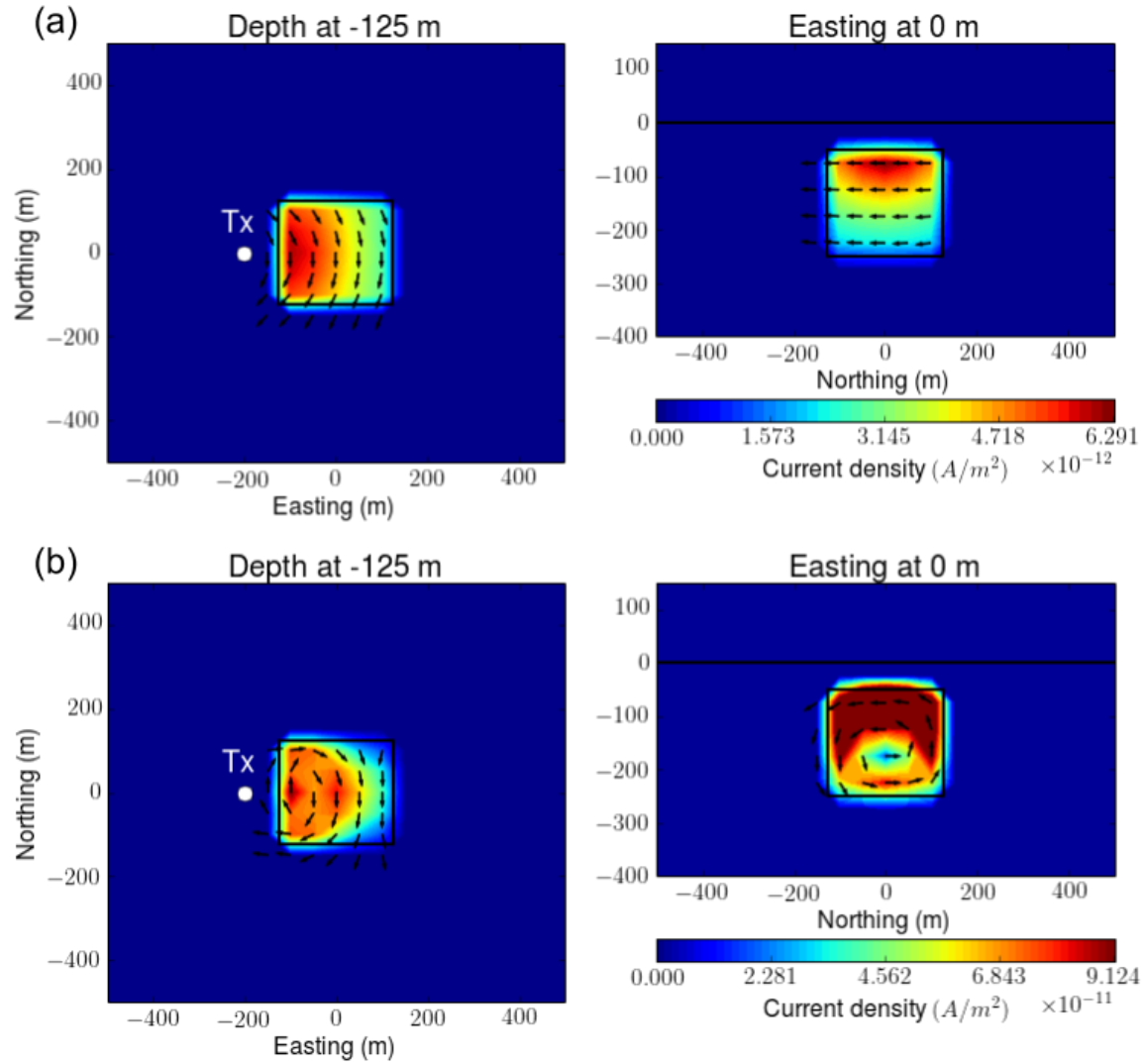


Figure 8. Maps of polarization currents: (a) canonical and (b) conductive models at 6.7 ms. Left and right panel show plan and section views at -125 m-depth and 0 m-easting, respectively. A transmitter is located at (-200 m, 0 m, 30 m). Black arrows and shaded value indicate the direction and amplitude of the current, respectively. Black solid outlines boundary of the surface or the chargeable body.

7.3 IP currents

The IP currents, as provided in equation (16), are given as

$$\vec{j}^{IP} = \sigma_{\infty} \vec{e}^{IP} + \vec{j}^{pol} \quad (59)$$

In most analyses, e.g. Smith et al. (1988), the term $\sigma_{\infty} \vec{e}^{IP}$ is neglected. In our work we have included this term but with an approximation that $\vec{e}^{IP} \approx -\nabla\phi$ (equation 30). Here we can investigate these approximations, and under what circumstances they hold. Using the forward modelling we can evaluate \vec{e}^{IP} . This field can be broken into galvanic and inductive parts using the Helmholtz decomposition: $\vec{e} = -\nabla\phi - \vec{a}$ so that $\vec{j}^{IP} = \vec{j}^{pol} - \sigma_{\infty}\phi^{IP} - \sigma_{\infty}\vec{a}^{IP}$. In our work we have included the effects from the scalar potential but neglected entirely any contribution from the vector potential.

To evaluate the relative importance of each of these terms we look at the contributions of each of these terms. for the three cases of canonical, conductive and resistive bodies. Figure 9 respectively show plan view maps of \vec{j}^{pol} , $-\sigma_{\infty}\vec{a}^{IP}$, and $-\sigma_{\infty}\phi^{IP}$ for (a) canonical, (b) conductive, and (c) resistive models at 0.86 ms.

For all three cases the polarization currents have the greatest strength in the body and the strength of these currents is largest in the conductive body and smallest in the resistive body. In all cases, the polarization currents are the largest contribution to \vec{j}^{IP} . The second column in Figure 9 is related to the scalar potential for the electric field or effectively to the galvanic currents. These exist both inside and outside the chargeable body. Again, these are largest for the conductive body. We note that inside the body, these currents are mostly in the opposite direction as the polarization currents. The third column is associated with the vector potential for the \vec{e}^{IP} and is associated with vortex currents. The effects of these currents has not been included in our linearized approximations. These currents are quite small for the canonical and resistive models. They are most noticeable for the conductive model where their amplitude starts to be comparable to the galvanic portion. We note that the direction of the vortex currents inside the body is the same as for the galvanic currents and opposite to the polarization currents. To add quantitative substance we evaluate \vec{j}^{IP} and its components at two locations in the body for conductive model. These are denoted by cross markers. For both points, polarization currents have the greatest strength and vortex currents are smaller than the galvanic currents. At a location on right-side, IP current is smaller than polarization current, because galvanic and vortex IP currents are in the opposite direction to the polarization currents.

The above figures provide insight about the three contributions \vec{j}^{IP} but of ultimate interest is the effect of these currents on the measured data. To examine contributions of the components of the IP current to the responses, we apply the Biot-Savart law to each current. It suffices to work with the conductive case. Figure 10 shows IP responses computed from the polarization current (stars),

Table 1. Amplitudes of decomposed IP currents at two marked points (crosses) shown in Figure 10(b). Units in A/m^2

Division	\vec{j}^{IP}	\vec{j}^{pol}	$-\sigma_{\infty} \vec{\nabla} \phi^{IP}$	$-\sigma_{\infty} \vec{a}^{IP}$
Left	5.0×10^{-10}	4.2×10^{-10}	7.4×10^{-11}	4.3×10^{-12}
Right	5.4×10^{-11}	1.2×10^{-10}	3.5×10^{-11}	3.3×10^{-11}

galvanic (rectangles) and inductive portions (circles) of the IP current. Here solid and empty markers show negative and positive signs, respectively. The polarization current has the major contribution to the IP response although it is larger than the true value. This overshoot is primarily negated by the galvanic portion of IP responses and further reduced because of the vortex currents. We notice that the contribution of the galvanic currents is generally larger than those due to the vortex currents except they are nearly equal near 0.4 ms. At 6.7 ms, the amplitude of the IP response due to the polarization current is about 130 percent of the true one, while galvanic portion is 30 percent. This result alludes Smith et al. (1988) assumption is still reasonable, whereas contribution of galvanic portion to IP datum is getting more important as time goes later. Inductive portion of IP responses always shows minor contribution compared to galvanic portion except for the time before 0.2 ms, and hence ignoring this inductive portion is reasonable for this case.

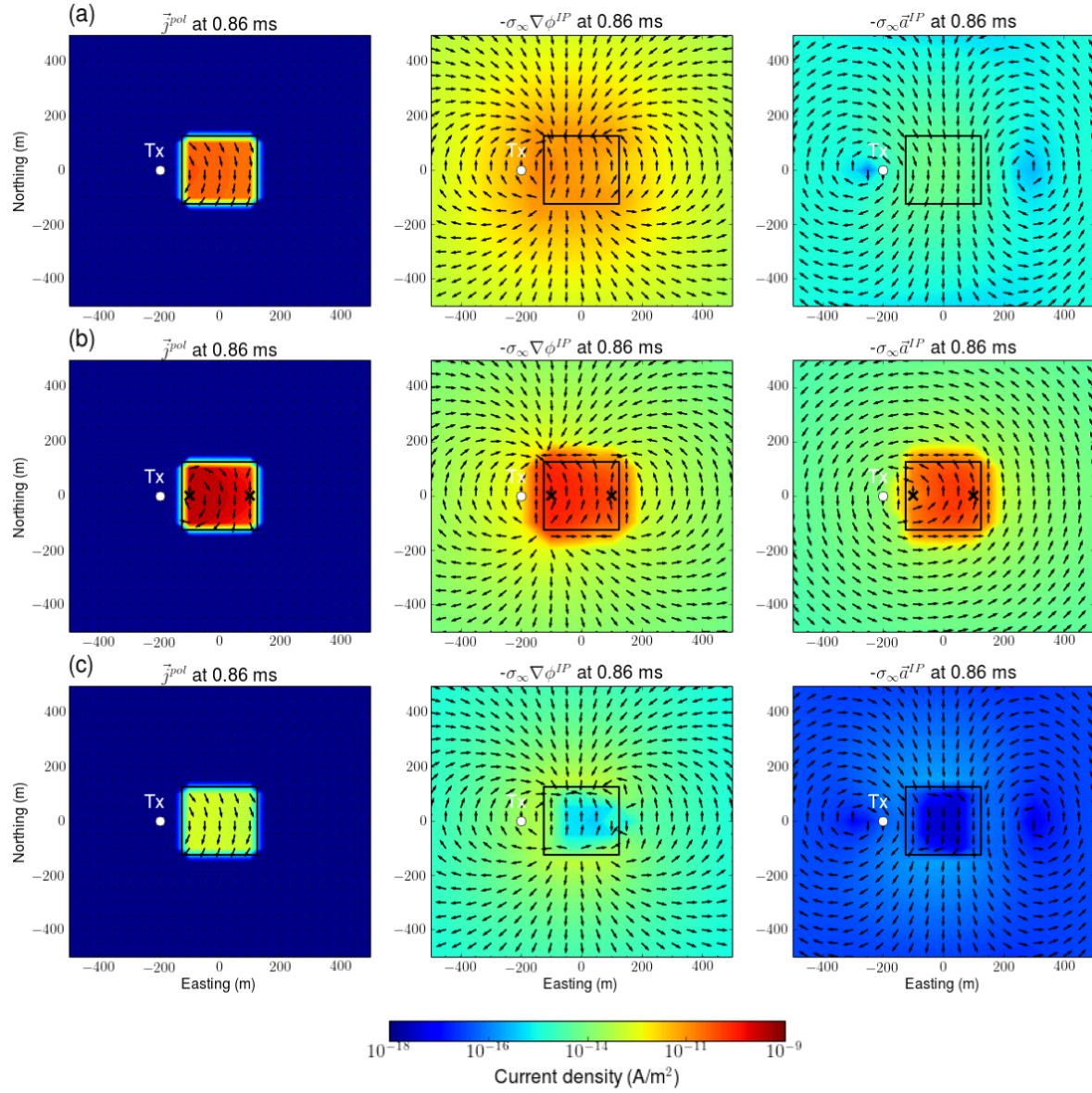


Figure 9. Decomposition of the IP currents as \vec{j}^{pol} (left panel), $-\sigma_{\infty} \vec{\nabla} \phi^{IP}$ (middle panel), and $-\sigma_{\infty} \vec{a}^{IP}$ (right panel) at 0.86 ms. Plan view maps of the currents at -125 m-depth are shown. (a) Canonical, (b) Conductive, and (c) Resistive cases.

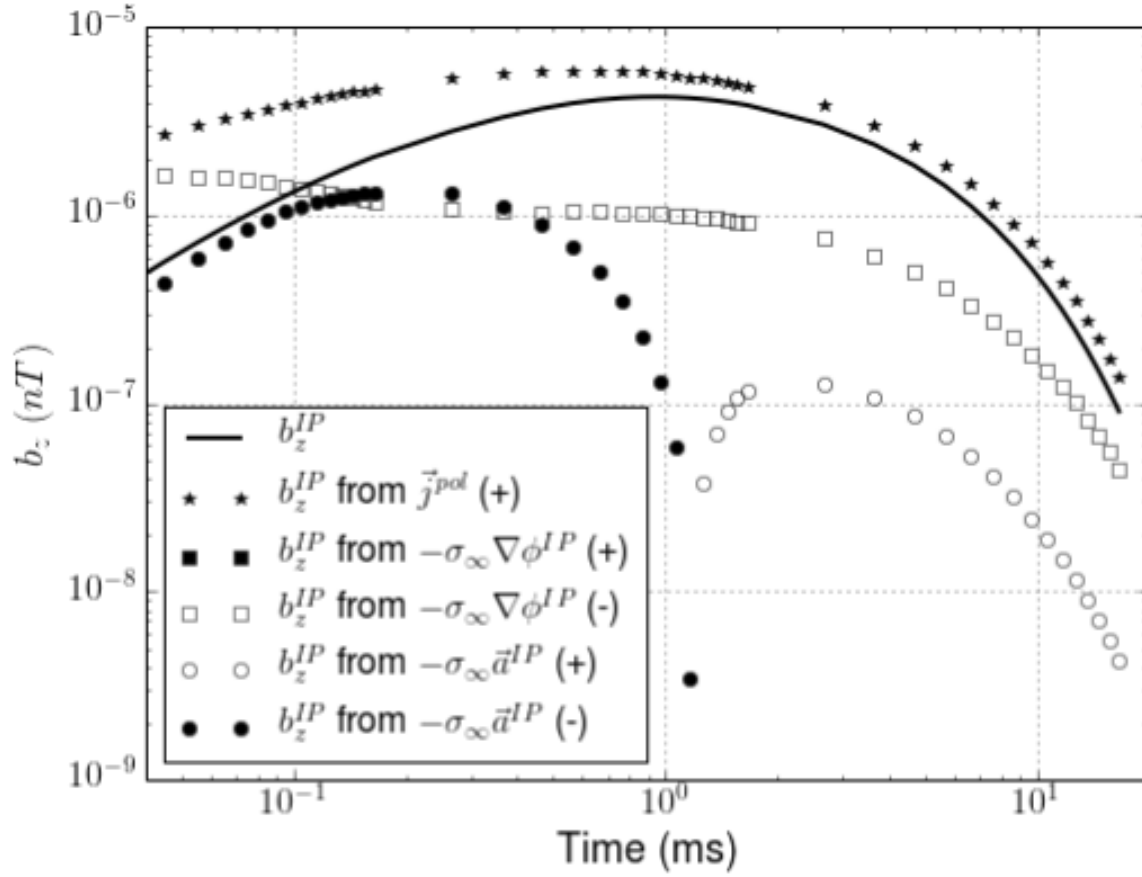


Figure 10. Comparisons of contributions of \vec{j}^{pol} , $-\sigma_\infty \vec{\nabla} \phi^{IP}$, and $-\sigma_\infty \vec{a}^{IP}$ to the observed IP responses. Solid line indicates true b_z^{IP} responses. Stars, rectangles, and circles correspondingly indicate each IP response generated by applying Biot-Savart law to \vec{j}^{pol} , $-\sigma_\infty \vec{\nabla} \phi^{IP}$, and $-\sigma_\infty \vec{a}^{IP}$. Empty and solid markers represent positive and negative values, respectively.

7.4 Validations of linearization

Forward modelling using our linear functional in equation (37) requires that we have adequately estimated the IP currents and evaluated their response using the Biot-Savart law. To validate this we first compute approximate IP currents using equation (33), and first compare them with the true IP currents. It suffices to work with the conductive model which is the most challenging. Figure 11 compares the true and approximate IP currents at 0.86 ms. The approximate IP currents match well, both in direction and amplitude, with the true IP currents both inside and outside the body. As shown in Figure 12 the agreement improves as time increases. Although not shown here, the canonical and resistive cases show good matches between the true and approximate IP currents at these times

Also, we next evaluate IP responses by applying the Biot-Savart law (equation (35)) to the approximate IP currents and compare them with the IP responses calculated by using the Biot-Savart law and the true IP currents. The results are shown in Figure 13. In addition we calculate the IP responses obtained by subtracting the fundamental response from the observations. The true responses, and the responses obtained from the Biot-Savart law using the true IP currents, are in very good agreement after 0.01 ms. This establishes the validity of the Biot-Savart computation. The responses obtained from using our approximate currents have slightly lower amplitude but overall they are in reasonable agreement with the true IP responses. Agreement between the various responses for the canonical and resistive cases are further improved.

Our linear functional reasonably explains d^{IP} data for the resistive case. However, possibility to observe IP response for the resistive case is significantly low considering its small amplitude compared to fundamental response.

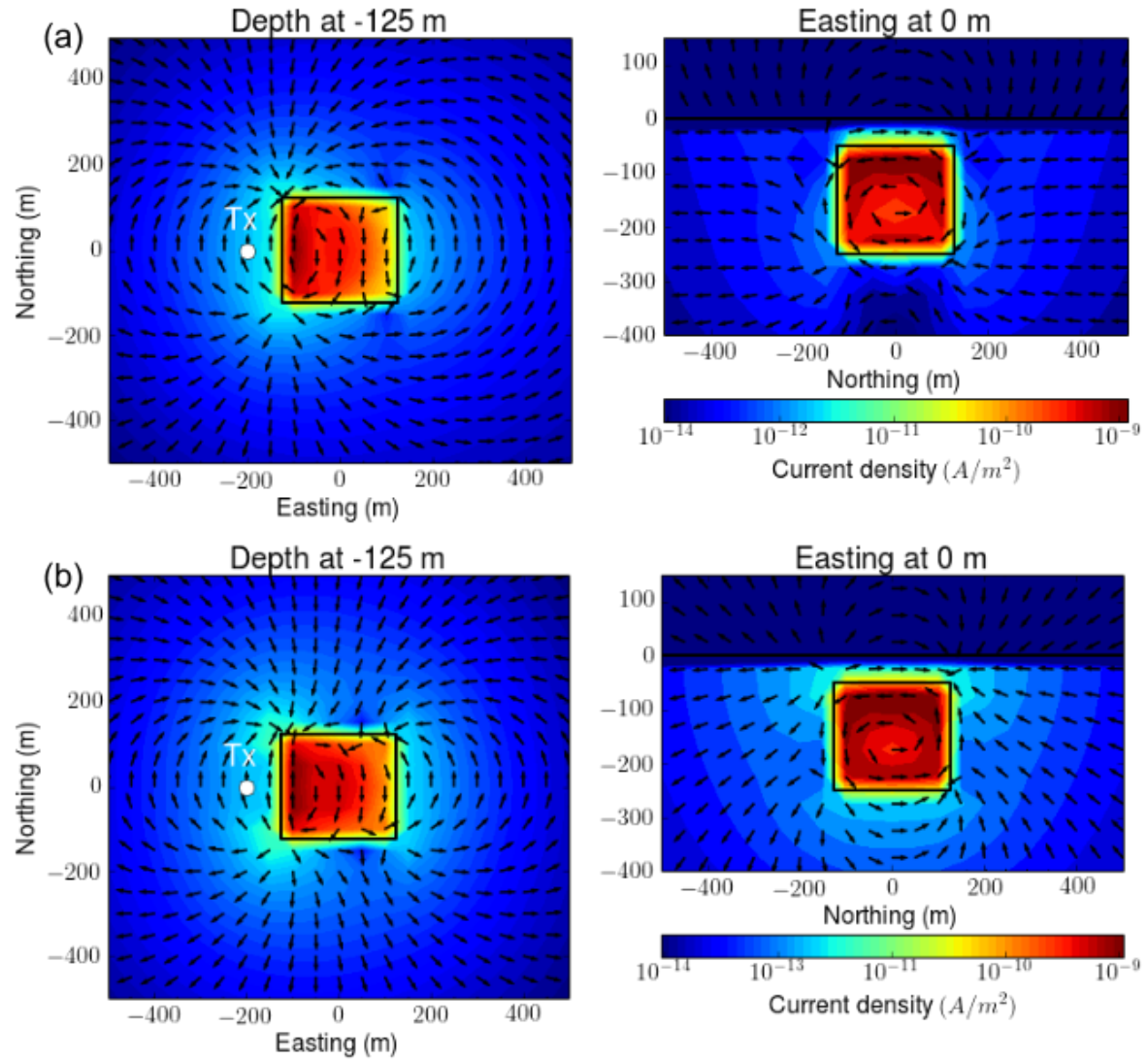


Figure 11. Interpolated maps of (a) true and (b) approximate IP currents at 0.86 ms. Left and right columns show plan and section view maps at -125 m-depth and 0 m-easting, respectively.

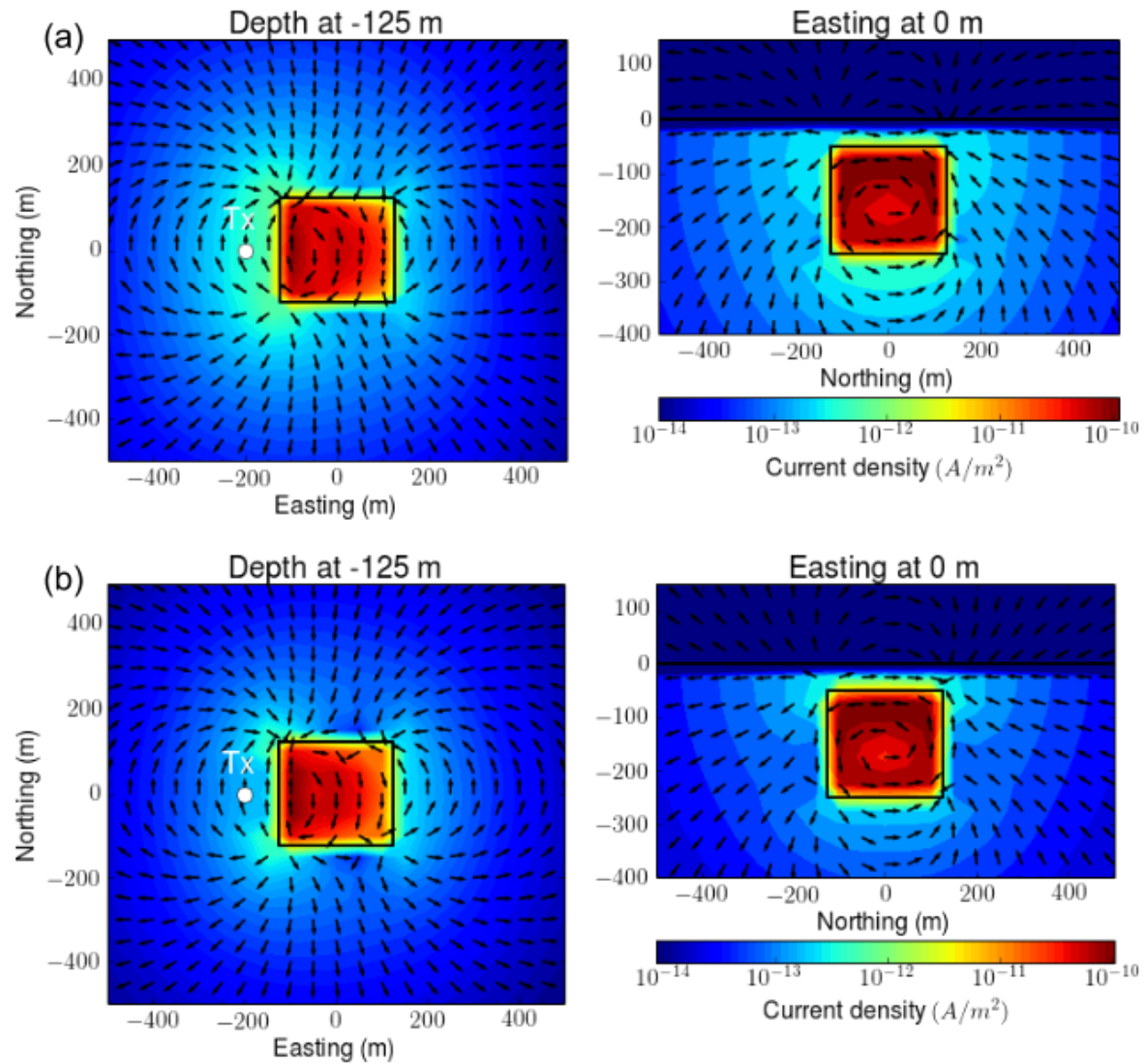


Figure 12. Interpolated maps of (a) true and (b) approximate IP currents at 6.7 ms. Left and right columns show plan and section view maps at -125 m-depth and 0 m-easting, respectively.

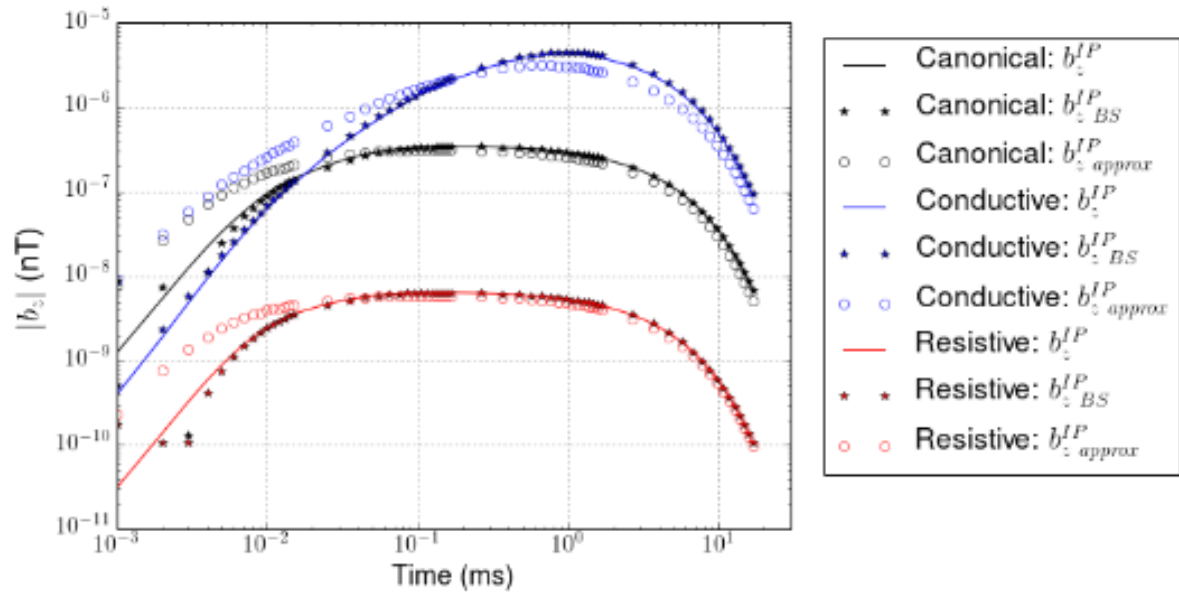


Figure 13. Comparison of true and approximate IP responses (b_z^{IP}). Black, blue, and red color respectively indicate canonical, conductive, and resistive cases. Solid lines indicate true b_z^{IP} computed by subtraction process and application of Biot-Savart to true IP current ($b_{z\ BS}^{IP}$). Empty circles presents approximate b_z^{IP} .

7.5 Effective pseudo-chargeability for ATEM data

In Section 7.5 we showed how to define an effective chargeability when we have multi-transmitters. For each pixel we have equation:

$$\tilde{\eta}_i(t) = \tilde{\eta}_i^I(t) \otimes w_i^e(t), \quad (60)$$

where $\tilde{\eta}_i^I(t)$ is the intrinsic chargeability associated with an individual pixel. The effective electric field function $w_i^e(t)$ is a linear combination of the fundamental electric fields due to the individual transmitters. We can calculate this and carry out the convolution to evaluate the pseudo-chargeability.

Using the effective pseudo-chargeability, we altered the problem as shown in equation (51), which later enables inverse problem recovering not pseudo-chargeability for each transmitter, but an effective pseudo-chargeability. Mathematical formulations to define the effective pseudo-chargeability is described in Section 6.3. There we derived the effective pseudo-chargeability by minimizing the squared difference between two quantities shown in equations (52) and (53). These quantities were not separate d^{IP} datum for each transmitter, but summation for contribution of a single pixel to d^{IP} data for all transmitters. Therefore, evaluating this effective pseudo-chargeability, computing IP responses at all transmitter locations, then comparing these to true IP responses are necessary procedure to test feasibility of the effective pseudo-chargeability. We only apply this to the conductive model.

For this test, we first evaluate effective $w^e(t)$ (equation (58)) then by convoluting $\tilde{\eta}^I(t)$ we compute effective $\tilde{\eta}(t)$. This requires calculating normalized weights shown in equation (55). Figure 14 show normalized weights at a single pixel located at (0 m, 0 m, -75 m). Reflecting the behaviour of the sensitivity function, the normalized weight is decaying from this pixel. With these weights, we compute effective $w^e(t)$ at the same pixel using equation (58). In Figure 15, we present $w^e(t)$ (dashed lines) for every transmitter and effective $w^e(t)$ (solid line). The effective $w^e(t)$ is dominantly affected by the $w^e(t)$ at the center transmitter location (solid circles). Values on early time for this $w^e(t)$ are zero, which are results of projection shown in equation (23). Similarly we evaluate effective $w^e(t)$ for every cell in the domain, and using this we compute effective pseudo-chargeability. With this we calculate approximate IP responses using linear functional (equation(37)). Figure 16 show the comparison of true and approximate IP responses on plan view map at 0.86 ms. Relative distribution of true and IP responses at different transmitter locations is compatible whereas the amplitude of d^{IP} is underestimated; the maximum amplitude of the true d^{IP} is ~ 2 times greater than that of the approximate d^{IP} . Similar trend was observed for the IP responses for a single transmitter as shown in Figure 13. At 0.86 ms, true IP response was ~ 1.5 times smaller than approximate one. After 0.86 ms, distribution of IP response on map view does not change significantly and both approximate d^{IP} responses show

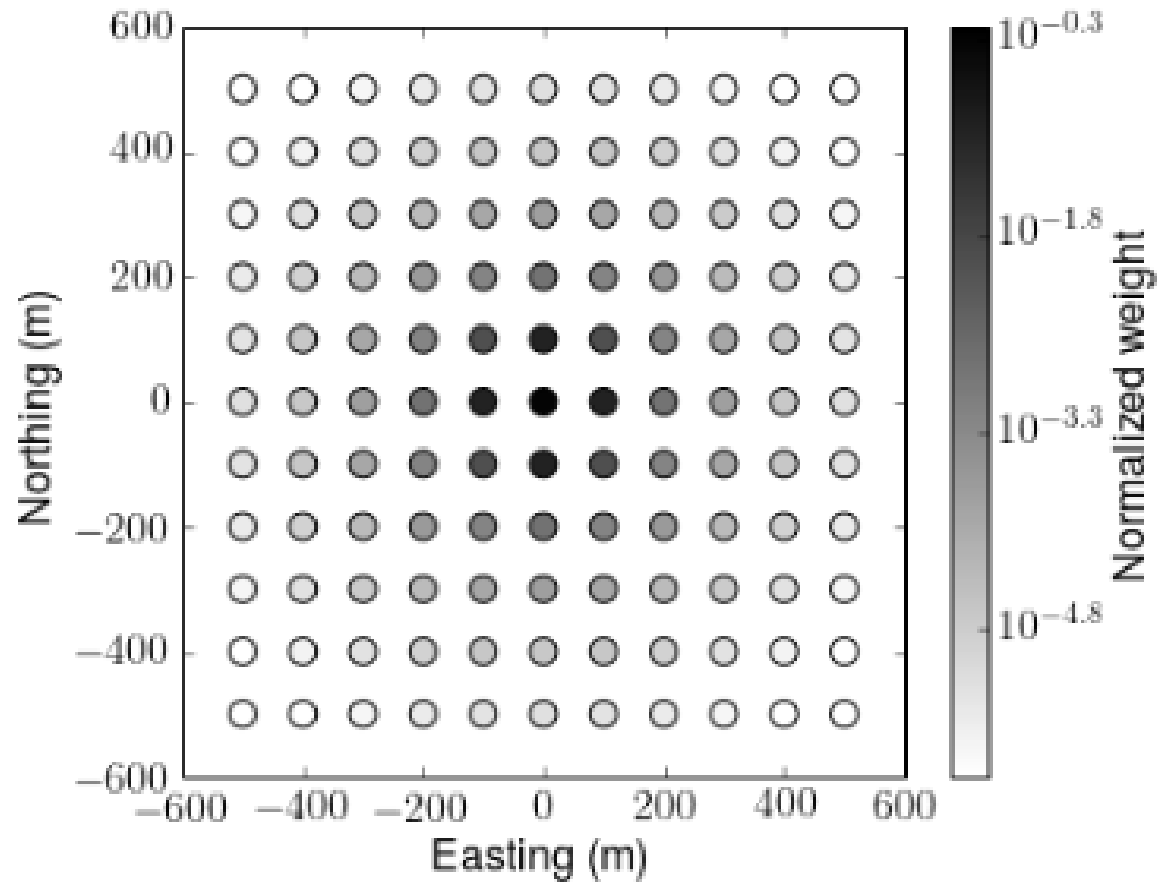


Figure 14. Normalized weights for the conductive case for all trasmitter locations. A single pixel located at (0 m, 0 m, -75 m) is used.

- 1 similar performances. Same anlyses was applied to canonical and resistive cases and showed similar
- 2 results, although we have not shown here.

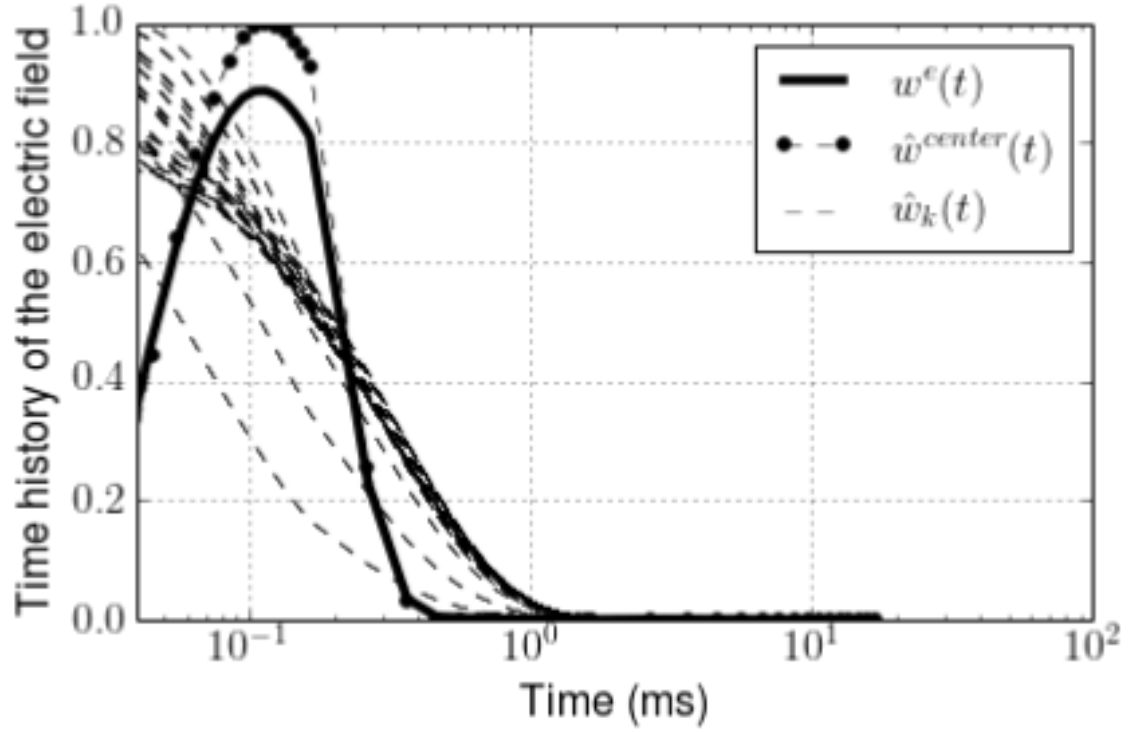


Figure 15. Effective $w^e(t)$ and $w_k^e(t)$ for all transmitter for the conductive case. A single pixel located at (0 m, 0 m, -75 m) is used. Solid line and dashed lines correspond to effective $w^e(t)$ and $w_k^e(t)$ for all transmitters ($k = 1, \dots, nTx$); w_k^e at the center transmitter located at (0 m, 0 m, 30 m) is marked as solid circles.

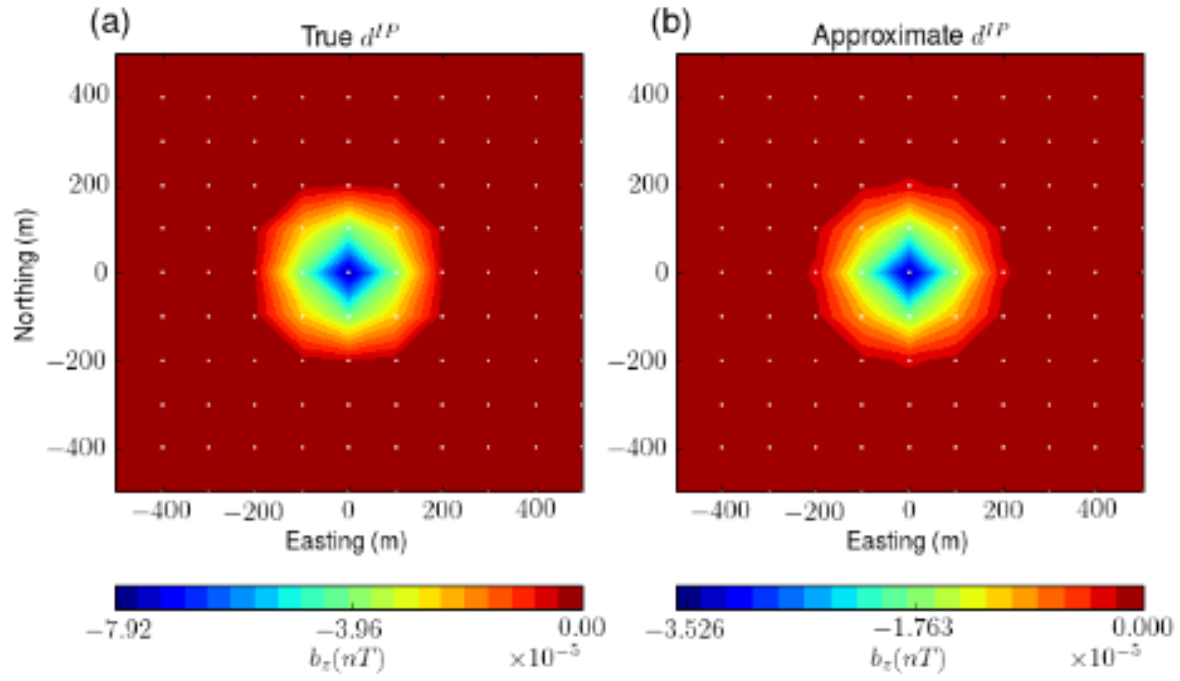


Figure 16. Comparison of true and approximate b_z^{IP} responses at 0.86 ms on plan view map.

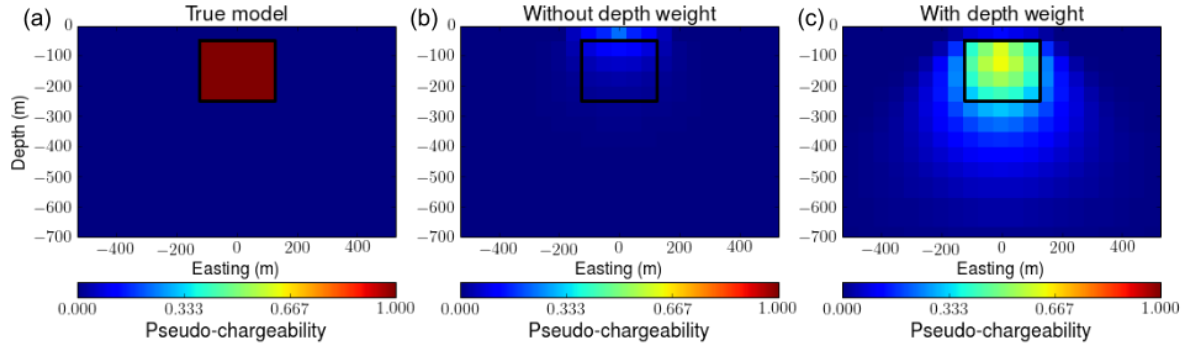


Figure 17. Effect of depth weight in 3D IP inversion. (a) True pseudo-chargeability model on vertical section at 0 m-northing. Recovered pseudo-chargeability models (b) without depth weight and (c) with depth weight.

7.6 3D IP inversions

Using our linearized sensitivity, we now proceed 3D IP inversion, which recovers a pseudo-chargeability given by equation (37). We limit our attention to the conductive case. For the computation of the sensitivity we use the true conductivity and then invert data at each successive time channels and recover 3D pseudo-chargeability at multiple times. Our 3D inversion is based upon (Oldenburg & Li 1994; Li & Oldenburg 2000), and it requires some choices for inversion parameters.

For data uncertainties, we used one percent of the maximum amplitude of the observed data ($0.01 \max(|\mathbf{d}^{obs}|)$). Coefficients for smallness and smoothness are set to $\alpha_s = 10^{-5}$ and $\alpha_x = \alpha_y = \alpha_z = 1$, respectively. The reference model is zero and we also applied a depth weighting and positivity constraint on the pseudo-chargeability. The need for a depth weighting arises because the sensitivity function J is primarily controlled by a $1/r^3$ decay associated with the Biot-Savart kernels. Thus an ATEM data set is not unlike commonly acquired magnetic data where it is well established that a depth weighting is required to image objects at depth. The following example illustrates this.

We first generate IP responses at a single time using the linear functional by assuming that the pseudo-chargeability is unity inside the body and zero outside, as shown in Figure 17(a). Figure 17(b) shows the recovered pseudo-chargeability without depth weighting. The recovered anomalous pseudo-chargeability is concentrated near the surface and the magnitude of the pseudo-chargeability is underestimated; it is ~ 0.2 rather than unity. By using the depth weighting shown in equation (42), the IP body is imaged closer to its true depth (Figure 17(c)). Also, the magnitude of the recovered pseudo-chargeability (~ 0.6) is closer to the true value than the result without depth weighting. Based on this analysis, we use the same depth weighting for our following examples.

7.6.1 *Incorrect conductivity*

The background conductivity plays a central role in our analysis. It is used in the EM decoupling process and it is also needed to compute the linearized sensitivities for inversion. Since we need to estimate this, usually through the inversion of EM survey data, it will never be correct. Here we explore some effects of an incorrect conductivity but the consequences are problem dependent.

We return to our conductive block in a halfspace and evaluate the d^{IP} data when the background is the true value ($\sigma_1 = 10^{-3}$ S/m) as well as a factor of two too large (2×10^{-3} S/m) and a factor of two too small (5×10^{-4} S/m). The data along a survey line are plotted in Figure 18.

We invert these three IP responses, and provide sections of the recovered pseudo-chargeability at 0 m-northing. Figure 19(a), (b) and (c) correspondingly show the recovered pseudo-chargeability when the conductivity is: the true value, too high, or too low. With the correct conductivity the geometry of the IP body is reasonably recovered. When the conductivity is too high, the d^{IP} have a negative bias that results in larger pseudo-chargeabilities and positive-valued artifacts near the IP body (Figure 19(b)). When the conductivity is too small, the IP data have a positive bias and this produces negative-valued artifacts near the IP body (Figure 19(c)). However, based on the definition of the pseudo-chargeability shown in equation (54), the sign of the pseudo-chargeability should be positive. By incorporating positivity as a constraint in the inversion we obtain the result in Figure 19(d). This is a much better result and comparison of the observed and predicted data for this case shown in Figure 20 clearly shows how this constraint prevents the fitting of positive residual fields. We shall use this positivity constraint for our following 3D IP inversion examples.

The background conductivity is also needed when computing the sensitivity function, since we need the reference electric field, which is dependent on conductivity. An incorrect conductivity will affect the sensitivity function as well. In order to test this, we compute the sensitivity matrix using a half-space conductivity model ($\sigma_\infty = \sigma_1$). Figure 21 compares the recovered pseudo-chargeability from the 3D IP inversion of the IP datum at 0.86 ms with the true and incorrect sensitivity function using half-space conductivity. There is not a large difference between the two inversions which suggests that an approximate conductivity may still provide sensitivities that are adequate for inversion. This parallels results from EIP where even an approximate conductivity can still yield good results when inverting the data. Thus there is some robustness in our sensitivity function with respect to an incorrect conductivity and even if we not have an accurate 3D conductivity model we can still apply our 3D IP inversion using half-space conductivity so long as the ATEM data includes distinctive IP response such as negative transients.

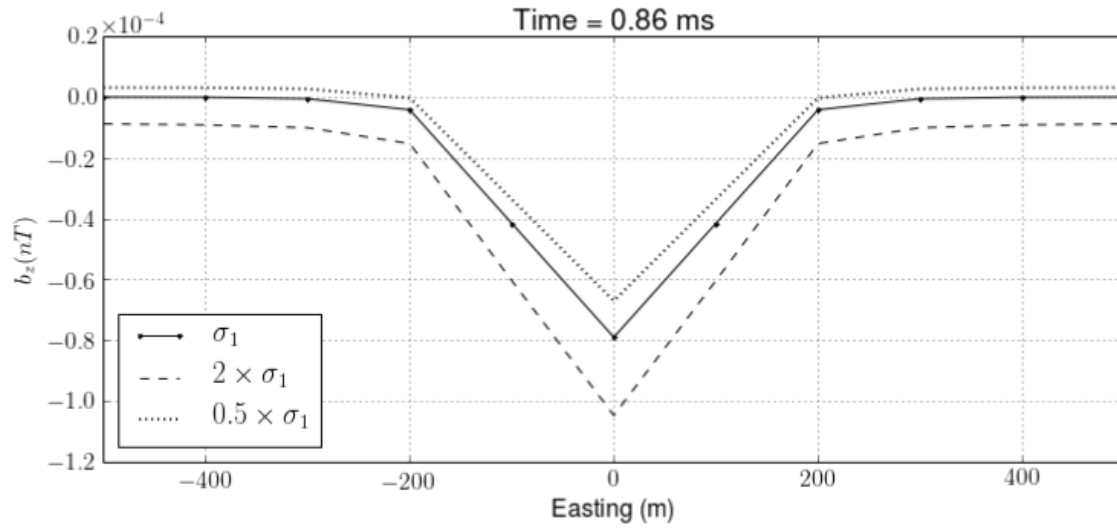


Figure 18. IP responses on a profile line at 0 m-northing. IP responses are computed from perturbed σ_∞ models. Half-space conductivity (σ_1) is perturbed two times higher or less resulting in overestimated (dotted line) and underestimated (dashed line) IP responses. Solid line shows the true IP response.

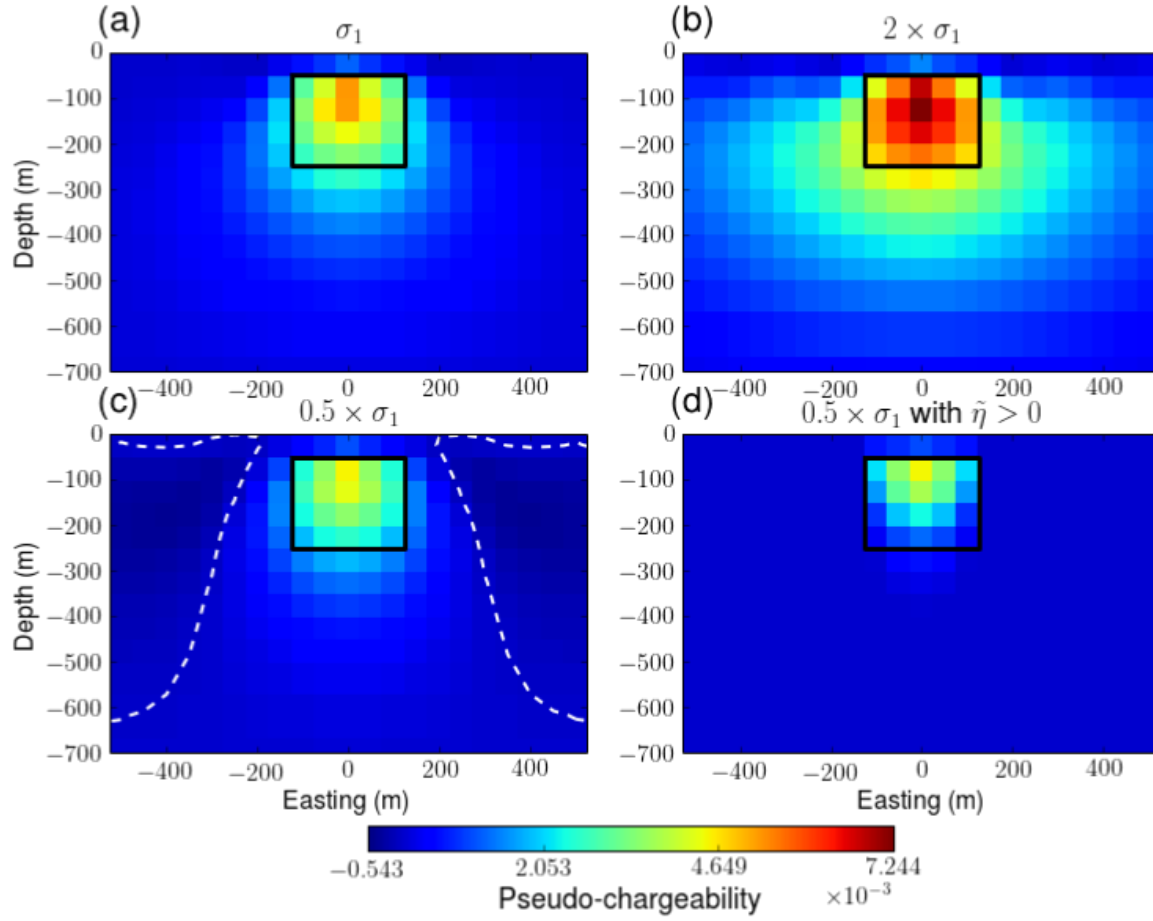


Figure 19. Recovered pseudo-chargeability sections from 3D IP inversions at 0 m-northing. (a) d^{IP} with true σ_1 . (b) d^{IP} with $2 \times \sigma_1$. (c) d^{IP} with $0.5 \times \sigma_1$. (d) d^{IP} with $0.5 \times \sigma_1$ and the positivity constraint on the pseudo-chargeability. White dashed lines contour zero-crossing lines.

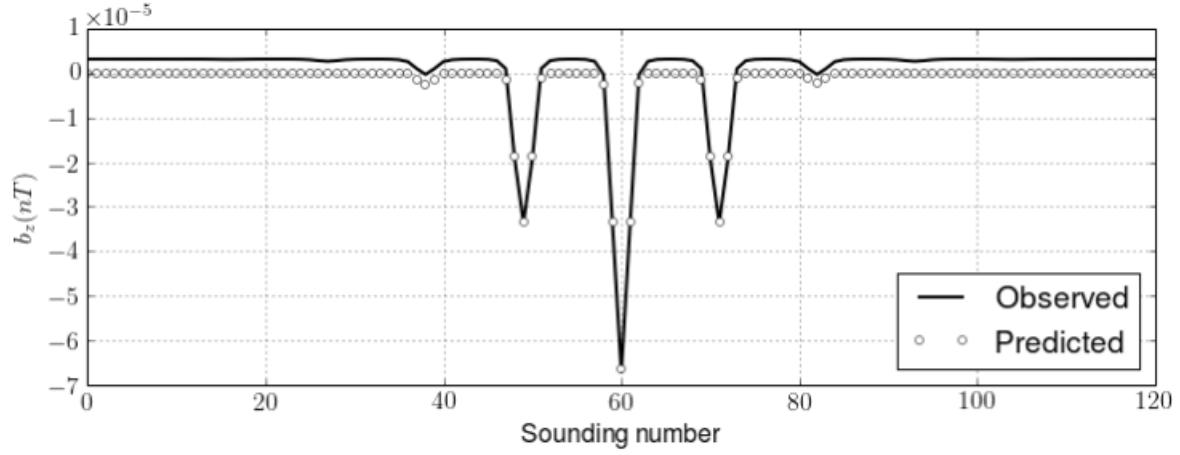


Figure 20. Comparison of the observed (solid line) and predicted (empty circles) data. d^{IP} response was generated with underestimated half-space conductivity ($0.5 \times \sigma_1$). The positivity constraint was used the 3D IP inversion.

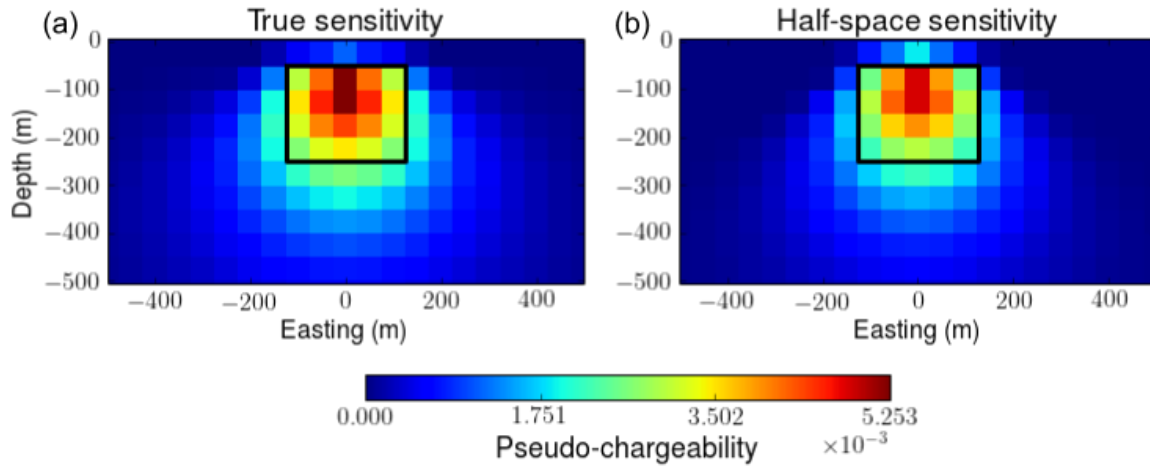


Figure 21. Recovered pseudo-chargeability sections from the 3D IP inversions at 0 m-northing. (a) True and (b) incorrect σ_∞ is used to compute sensitivity function. For the incorrect sensitivity we used half-space conductivity (σ_1).

7.6.2 *Extracting intrinsic IP parameters*

By applying our inversion to each time channel of d^{IP} data separately, we can recover 3D distributions of pseudo-chargeability at multiple times. Pseudo-chargeability at each time carried different information about the state of polarization and we can use these to recover information about intrinsic IP parameters. Diverse time-dependent conductivity models such Cole-Cole model and stretched-exponential can be used for this interpretation. We use the Cole-Cole model with $c=1$. We parametrize pseudo-chargeability at a single pixel in terms of chargeability and time constant as described in Section 6.2, and solve a small inverse problem. This parallels (Yuval & Oldenburg 1997; Hördt et al. 2006).

As an example, use the conductive and chargeable block presented in the previous section and we invert 14 time channels of data ranging from 1-10 ms. The true σ_{∞} model is used for both evaluation of IP datum and sensitivity function. The recovered pseudo-chargeability from one of the 14 inversions is shown in Figure 21a. In that pseudo-chargeability model, we choose cells having greater pseudo-chargeability value than 0.001, and estimate the time constant (τ) and chargeability (η) of each cell separately. A forward kernel for this inversion is shown in equation (43), which requires effective $w^e(t)$. The effective $w^e(t)$ for this pixel are shown in Figure 15, and this is used to evaluate the forward kernel for the inversion. Figure 22a and b correspondingly show the estimated time constant and chargeability on section view maps. Estimated time constant values show reasonable values in overall region compared to the true value: 0.005. Near upper boundary of the chargeable body, estimated chargeability is around 0.1, which is 2 times less than the true value: 0.2, and away from this region estimated values are considerably underestimated. This result is possibly related to greater sensitivity of IP response for the ATEM data on near surface chargeable medium. In Figure 23, we also provide time decay of the observed and predicted data at a single pixel marked as black empty rectangles in Figure 22. The estimated time constant (τ_{est}) and chargeability (η_{est}) for this pixel are 0.0044 and 0.11, respectively. These results imply more stability on recovering time constant than chargeability with our approach. Although the same experiments for canonical and resistive cases have been treated, we have not shown here for the brevity of the article. Similar to conductive case, we recovered reasonable time constant, whereas the recovered chargeability is underestimated for two other cases.

We used a simple interpretation method to extract Cole-Cole parameters from multiple times of recovered pseudo-chargeability, which are products of our IP inversion, to glimpse a possibility on this problem. However, more sophisticated methodology and systematic analyses on extracting this intrinsic IP information from d^{IP} data are necessary as a future study.

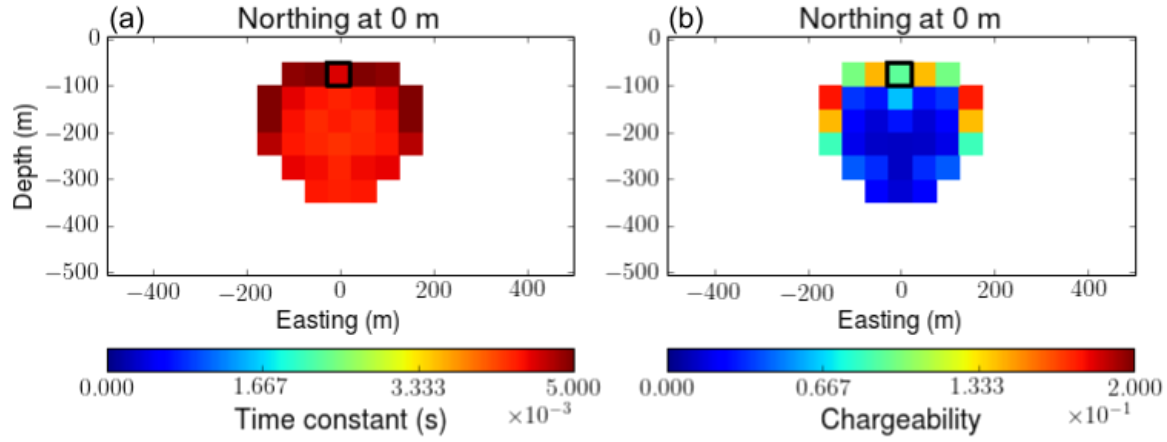


Figure 22. Section views of recovered (a) time constant and (b) chargeability. Any region where the pseudo-chargeability shown in Figure 21a is smaller than 0.001 is ignored in this analysis, and blanked.

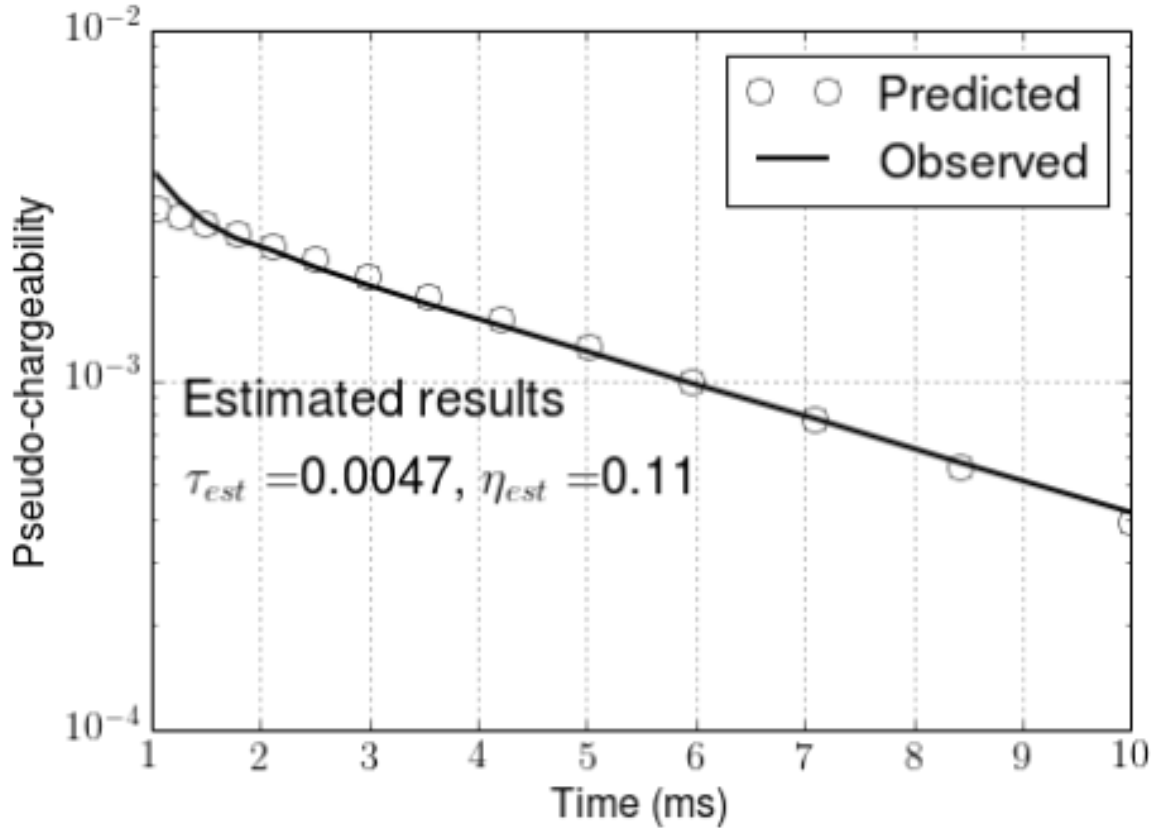


Figure 23. Comparisons of the observed and predicted pseudo-chargeability at a single pixel in a chargeable body. Empty and solid circles indicate predicted pseudo-chargeabilities using two different $w_{avg}^e(t)$ for the choices of normalized weights: a single cell and all cells in a chargeable block, respectively. Estimated time constant and chargeability for each inversion are expressed as τ_{est} and η_{est} , respectively.

8 CONCLUSIONS

In this paper, we have introduced an IP inversion procedure for the TEM data, especially for the inductive source. This includes three main steps: 1) subtraction of the fundamental response from the observation, 2) linearization of the IP response as a function of the pseudo-chargeability, and 3) restoration of 3D pseudo-chargeability at multiple times, and further interpretation of the pseudo-chargeability to extract intrinsic IP parameters like Cole-Cole model. We used ATEM survey to test our IP inversion procedure.

Assuming that we can recover reasonable 3D conductivity by inverting TEM data with exception of the IP-contaminated data, evaluation of the first step allows us to identify IP responses embedded in the observation. By taking analogy from the EIP case, we effectively linearize ISIP response in time domain as a function of the pseudo-chargeability. This pseudo-chargeability is defined as a fraction of the polarization current and the reference current, which may provide us the strength of the IP effect. Different from the EIP case, the polarization charge buildup does not reach to the steady-state for the ISIP case due to the absence of steady-state electric field for inductive source. This fundamental difference is carefully incorporated to the linearization with a proper choice of the reference electric field. Numerical tests on the approximate IP current and responses demonstrated the capability of the linearized kernel for various conductivity structures: canonical, conductive, and resistive cases. Our linearization is effective at certain late time when the IP effect is considerable to the EM effect, which may occur in the discharging phase.

In order to formulate 3D IP inversion, we derived an effective pseudo-chargeability, which represents pseudo-chargeability of every transmitter, and tested with numerical simulation. Based on this, we inverted IP responses at multiple times, separately, and recovered pseudo-chargeability at those times. Due to the possible lack of intrinsic depth resolution in our kernel for the ATEM survey, the depth weighting is used in the inversion. Our 3D IP inversion recovered reasonable geometric shape and location of the chargeable body. Because we may not recover true conductivity in practice, we tested possible effects of incorrect conductivity. Two important places where we use conductivity are EM decoupling and sensitivity function. By designing two situations where we have positive or negative residual field in the IP response, we investigated the effect of incorrect conductivity in the IP response and the 3D IP inversion. For the positive residual field, we showed that positivity constraint can be effectively used to prevent fitting those residual field. In addition, even with a poor sensitivity function computed using half-space conductivity model, we recovered important information of the chargeable body such as geometric shape and location. Finally, by interpreting recovered pseudo-chargeability at the center pixel of the IP body in time, we extracted Cole-Cole parameters: τ and η

by assuming $c = 1$. Estimated τ was close to true one whereas η was underestimated. This suggests a potential to extract intrinsic IP parameters from the recovered pseudo-chargeability.

Our IP inversion procedure provides a framework that one can recover 3D distribution of the pseudo-chargeability, and possibly extraction of intrinsic IP parameters with post-processings of the pseudo-chargeability. Because our inversion procedure requires 3D distribution of σ_∞ , which may not be trivial in some cases, this should be carefully investigated in the future for practical application of our inversion methodology. In addition, our numerical examples was only treated the ATEM survey, even though application to different types of inductive source TEM survey such as Large-loop TEM may have different aspects that we need to consider. However, still important items including EM decoupling, linearization and 3D IP inversion, which have been come up with and carefully tested in this study, will be fundamental backgrounds of following future studies about the ISIP in time domain.

APPENDIX A: DISCRETIZATION OF STEADY-STATE MAXWELL'S EQUATIONS

As shwon equation (31), computation of our linearized kernel requires solving steady-state Maxwell's equations. We discretize this system using mimetic finite volume (FV) method with weak formulation (Haber (2014)). For the discretization, we assume that the electric field \vec{e} is discretized by grid function \mathbf{e} on cell edges and magnetic flux density \vec{b} is discretized by grid fuction \mathbf{b} on cell faces. Electrical potential ϕ is discretized by grid fuction ϕ on cell nodes. For clear representation of the derivation, recall Maxwell's equations in steady state as

$$\vec{j} = \sigma_\infty \vec{e} = -\sigma_\infty \vec{\nabla} \phi, \quad (\text{A.1})$$

$$-\nabla \cdot \vec{j} = \nabla \cdot \vec{j}_s, \quad (\text{A.2})$$

$$\vec{j}|_{\partial\Omega} \cdot \hat{n} = 0, \quad (\text{A.3})$$

where $\partial\Omega$ indicates boundary surface of the system and \hat{n} is the normal vector of the boundary surface. Weak form of those equations can be written as

$$(\vec{j}, \vec{w}) + (\sigma_\infty \vec{\nabla} \phi, \vec{w}) = 0, \quad (\text{A.4})$$

$$-(\vec{j}, \vec{\nabla} \psi) = (\vec{j}_s, \vec{\nabla} \psi). \quad (\text{A.5})$$

The inner products (\vec{j}, \vec{w}) , $(\sigma_\infty \vec{\nabla} \phi, \vec{w})$, $(\vec{j}, \vec{\nabla} \psi)$ and $(\vec{j}_s, \vec{\nabla} \psi)$ are edge based products. Here we define the inner product as

$$(\vec{a}, \vec{b}) = \int_{\Omega} \vec{a} \cdot \vec{b} dv, \quad (\text{A.6})$$

where Ω is the volume of the system. By discretizing $\vec{\nabla}$ operator and the inner product in space, we obtain

$$\mathbf{M}^e \mathbf{j} + \mathbf{M}_{\sigma_\infty}^e \mathbf{G} \phi = 0, \quad (\text{A.7})$$

$$-\mathbf{G}^T \mathbf{M}^e \mathbf{j} = \mathbf{G}^T \mathbf{M}_{\sigma_\infty}^e \mathbf{j}_s, \quad (\text{A.8})$$

where \mathbf{M}_i^e is the mass matrices, which discretize the edge based inner product (Haber (2014)). This inner products are defined as

$$\mathbf{M}_i^e = \mathbf{diag}(\mathbf{A}_c^{eT} \mathbf{diag}(\mathbf{v}) \mathbf{i}). \quad (\text{A.9})$$

Here, \mathbf{i} indicates a grid function on cell center like σ_∞ , and \mathbf{v} is the grid function for the cell volume. The averaging matrix \mathbf{A}_c^e averages discrete function defined on the edges to the cell center. The mass matrix \mathbf{M}^e without subscript i indicates that \mathbf{i} is equal to the identity column vector of which all elements are one. By substituting equation (A.7) to (A.8), we have

$$\mathbf{A}_{\sigma_\infty} \phi = \mathbf{rhs}^{DC}, \quad (\text{A.10})$$

where $\mathbf{A}_{\sigma_\infty} = \mathbf{G}^T \mathbf{M}_{\sigma_\infty}^e \mathbf{G}$ and $\mathbf{rhs}^{DC} = \mathbf{G}^T \mathbf{M}^e \mathbf{j}_s$.

APPENDIX B: DISCRETIZATION OF THE LINEARIZED KERNEL

To obtain linear form of equation shown in equation (37), we first discretize Biot-Savart law shown in equations (35) and (36). In our discretization \vec{j}^{IP} and $\tilde{\eta}$ are defined on the cell center, and those for each time channel are constant in a cell volume, whereas \vec{e}^{ref} is defined on the cell edges. We define the number of cells and edges in 3D space as n_C and n_E , respectively. Discretized IP current density, $\mathbf{j}_{cc}^{IP} \in \mathbb{R}_1^{3n_C}$, and defined on the cell center, since \vec{j}^{IP} has three components, we first discretize integration operator including cross product ($\int_v \frac{\mathbf{x} \times \hat{\mathbf{r}}}{r^2} dv$) as

$$\mathbf{G}_{Biot} = \begin{bmatrix} \mathbf{e}^T & \mathbf{0} & \mathbf{0} \\ \mathbf{0} & \mathbf{e}^T & \mathbf{0} \\ \mathbf{0} & \mathbf{0} & \mathbf{e}^T \end{bmatrix} \begin{bmatrix} \mathbf{0} & \mathbf{S}_z & -\mathbf{S}_y \\ -\mathbf{S}_z & \mathbf{0} & \mathbf{S}_x \\ \mathbf{S}_y & -\mathbf{S}_x & \mathbf{0} \end{bmatrix}, \quad (\text{B.1})$$

where

$$\mathbf{S}_l = \mathbf{diag}(\mathbf{v} \oplus \mathbf{r}_l \oplus \frac{1}{r^2}), \quad l = x, y, z$$

and the electric field, $\mathbf{e} \in \mathbb{R}_1^{n_E}$ is a column vector, $\mathbf{diag}(\cdot)$ is the diagonal matrix and \oplus is the Hadamard product. Then we discretize \vec{j}^{IP} shown in equation (33) as

$$\mathbf{j}_{cc}^{IP}(t) = \mathbf{S} \mathbf{diag}(\mathbf{e}_{max}^F) \mathbf{A}_c^{eT} \mathbf{diag}(\mathbf{v}) \mathbf{diag}(\sigma_\infty) \tilde{\eta}(t), \quad (\text{B.2})$$

where

$$\mathbf{S} = \mathbf{A}_{ccv}^e \mathbf{M}^{e-1} [\mathbf{M}_{\sigma_\infty}^e \mathbf{G} \mathbf{A}_{\sigma_\infty}^{-1} \mathbf{G}^T - \mathbf{I}] \text{diag}(\mathbf{e}_{max}^F) \mathbf{A}_c^{eT} \text{diag}(\mathbf{v}) \text{diag}(\sigma_\infty). \quad (\text{B.3})$$

and \mathbf{A}_{ccv}^e is discrete averaging matrix from edge to cell center with consideration of three component vector: $\in \mathbb{R}_{nE}^{3nC}$. Thus, we can have linear equation for k^{th} time channel as

$$\mathbf{b}_i^{IP} = \mathbf{G}_{Biot} \mathbf{S} \tilde{\eta}_i,$$

where subscript i indicates i^{th} time channel. Finally, by letting

$$\mathbf{J} = -\mathbf{G}_{Biot} \mathbf{S}, \quad (\text{B.4})$$

we have

$$\mathbf{b}_i^{IP} = \mathbf{J} \tilde{\eta}_i, \quad (\text{B.5})$$

where \mathbf{J} is the Jacobian matrix of the linear equation, and since \mathbf{J} is static, we also obtain

$$-\frac{\partial \mathbf{b}^{IP}}{\partial t} \Big|_i = \mathbf{J} \left(-\frac{\partial \tilde{\eta}}{\partial t} \Big|_i \right). \quad (\text{B.6})$$

REFERENCES

- Chen, J. & W. Oldenburg, D., 2003. 3-D inversion of magnetic induced polarization data, *ASEG Extended Abstracts*, **2003**(1), 1–11.
- Cole, K. S. & Cole, R. H., 1941. Dispersion and absorption in dielectrics i. alternating current characteristics, *The Journal of Chemical Physics*, **9**(4).
- ElKaliouby, H. & Eldiwany, E., 2004. Transient electromagnetic responses of 3D polarizable body, *GEO-PHYSICS*, **69**(2), 426–430.
- Fink, J., McAlister, E., Sternberg, B., Wieduwilt, W., & Ward, S., 1990. *Induced Polarization Applications and Case Histories*, Society of Exploration Geophysicists.
- Flis, M. F., Newman, G. A., & Hohmann, G. W., 1989. Induced polarization effects in timedomain electromagnetic measurements, *GEOPHYSICS*, **54**(4), 514–523.
- Haber, E., 2014. *Computational Methods in Geophysical Electromagnetics*, Society for Industrial and Applied Mathematics, Philadelphia, PA.
- Hördt, A., Hanstein, T., Hönig, M., & Neubauer, F. M., 2006. Efficient spectral IP-modelling in the time domain, *Journal of Applied Geophysics*, **59**(2), 152–161.
- Kang, S. & W. Oldenburg, D., 2015. Recovering IP information in airborne-time domain electromagnetic data, *ASEG Extended Abstracts*, **2015**(1), 1–4.
- Kang, S., Noh, K., Seol, S. J., & Byun, J., 2014. mCSEM inversion for CO2 sequestration monitoring at a deep brine aquifer in a shallow sea.
- Kang, S., W. Oldenburg, D., & S. McMillan, M., 2015. 3D IP Inversion of Airborne EM data at Tli Kwi Cho, *ASEG Extended Abstracts*, **2015**(1), 1–4.

- 1 Kelley, C. T., 1999. *Iterative Methods for Optimization*, Society for Industrial and Applied Mathematics.
- 2 Kemna, A., Binley, A., Cassiani, G., Niederleithinger, E., Revil, A., Slater, L., Williams, K. H., Orozco, A. F.,
- 3 Haegel, F. H., Hördt, A., Kruschwitz, S., Leroux, V., Titov, K., & Zimmermann, E., 2012. An overview
- 4 of the spectral induced polarization method for near-surface applications, *Near Surface Geophysics*, **10**(6),
- 5 453–468.
- 6 Kohlrausch, R., 1854. Theorie des elektrischen Rückstandes in der Leidener Flasche, *Annalen der Physik*,
- 7 **167**(2), 179–214.
- 8 Kratzer, T. & Macnae, J., 2012. Induced polarization in airborne EM, *Geophysics*, **77**(5), E317–E327.
- 9 Li, Y. & Oldenburg, D. W., 1996. 3-d inversion of magnetic data, *GEOPHYSICS*, **61**(2), 394–408.
- 10 Li, Y. & Oldenburg, D. W., 2000. 3-D inversion of induced polarization data, *Geophysics*, **65**(6), 1931–1945.
- 11 Marchant, D., Haber, E., & Oldenburg, D. W., 2012. Inductive source induced polarization, *Geophysical*
- 12 *Journal International*, **192**(2), 602–612.
- 13 Marchant, D., Haber, E., & Oldenburg, D. W., 2014. Three-dimensional modeling of ip effects in time-domain
- 14 electromagnetic data, *GEOPHYSICS*, **79**(6), E303–E314.
- 15 Oldenburg, D. & Li, Y., 1994. Inversion of induced polarization data, *GEOPHYSICS*, **59**(9), 1327–1341.
- 16 Oldenburg, D. W. & Li, Y., 2005. 5. *Inversion for Applied Geophysics: A Tutorial*, chap. 5, pp. 89–150.
- 17 Oldenburg, D. W., Kang, S., & Marchant, D., ????. *Inversion of time domain IP data from inductive sources*,
- 18 chap. 2, pp. 9–12.
- 19 Pelton, W., Ward, S., Hallof, P., Sill, W., & Nelson, P., 1978. MINERAL DISCRIMINATION AND RE-
- 20 MOVAL OF INDUCTIVE COUPLING WITH MULTIFREQUENCY IP, *Geophysics*, **43**(3), 588–609.
- 21 Routh, P. S. & Oldenburg, D. W., 2001. Electromagnetic coupling in frequency-domain induced polarization
- 22 data: a method for removal, *Geophysical Journal International*, **145**(1), 59–76.
- 23 Seigel, H., 1959. Mathematical formulation and type curves for induced polarization, *GEOPHYSICS*, **24**(3),
- 24 547–565.
- 25 Seigel, H., 1974. The magnetic induced polarization (mip) method, *GEOPHYSICS*, **39**(3), 321–339.
- 26 Smith, R. S. & Klein, J., 1996. A special circumstance of airborne induced polarization measurements, *GEO-*
- 27 *PHYSICS*, **61**(1), 66–73.
- 28 Smith, R. S., Walker, P., Polzer, B., & West, G. F., 1988. The time-domain electromagnetic response of
- 29 polarizable bodies: an approximate convolution algorithm, *Geophysical Prospecting*, **36**(April), 772–785.
- 30 Weidelt, P., 1982. Response characteristics of coincident loop transient electromagnetic systems, **47**(Septem-
- 31 ber), 1325–1330.
- 32 Yuval & Oldenburg, D., 1997. Computation of colecole parameters from ip data, *Geophysics*, **62**(2), 436–448.